

NATIONAL UNIVERSITY OF HO CHI MINH CITY  
UNIVERSITY OF SCIENCE  
FACULTY OF PHYSICS - ENGINEERING PHYSICS

ooo

UNDERGRADUATE THESIS

Thesis title:

Hofstadter butterfly in transition metal  
dichalcogenide monolayers

---

Student: Tran Khoi Nguyen  
Supervisor: Dr. Huynh Thanh Duc

Ho Chi Minh City, 2025

**NATIONAL UNIVERSITY OF HO CHI MINH CITY  
UNIVERSITY OF SCIENCE  
FACULTY OF PHYSICS - ENGINEERING PHYSICS**

**UNDERGRADUATE THESIS**

**Thesis title:**

**Hofstadter butterfly in transition metal  
dichalcogenide monolayers**

Major code: 7440102

Specialization: Theoretical Physics

---

**Student: Tran Khoi Nguyen  
Supervisor: Dr. Huynh Thanh Duc**

Ho Chi Minh City, 2025

## **GUARANTEE**

I guarantee to independently conducting the calculation of the Hofstadter butterfly of an ideal two-dimensional system of MoS<sub>2</sub> for my bachelor thesis, under the supervision of Dr. Huynh Thanh Duc.

The contexts are included in this graduation thesis are totally accurate and honest.

**STUDENT**  
*(Signature)*

Tran Khoi Nguyen

## ACKNOWLEDGMENTS

This thesis would not have been possible without the help and support of a large number of individuals. Firstly, I would like to thank my family members, especially my beloved mother and my sister, who have totally encouraged me on my path of becoming a scientist and helped me tremendously in all ways possible. Without them, I would not have enough much confidence to finish this. Thank you.

I am deeply greeted to my supervisor Dr. Huynh Thanh Duc from the Institute of Physics, Ho Chi Minh city, who taught me not only knowledges, gave me advise but also wholeheartedly encouraged and guided me every steps of the way. I would like to thank Master Le Minh Chau from the Institute of Physics and Vo Chau Duc Phuong from ICTP, who helped me at the very first step of this thesis. I would also like to acknowledge with gratitude to Dr. Vu Quang Tuyen, Dr. Vo Quoc Phong and Dr. Nguyen Huu Nha from the Department of Theoretical Physics. They have trully inspired me on the way becoming a physicist.

Finally, I would like to thank my colleagues at the University of Science including Dao Duy Tung, Le Quoc Duy, Ho Ngo Thanh Khoa, Pham Hoang Minh Quang, Truong Anh Duy, Pham Nguyen Thanh Dat.

*Ho Chi Minh city, July, 2025*

**Tran Khoi Nguyen**

## TABLE OF CONTENTS

<b>1</b>	<b>INTRODUCTION</b>	<b>1</b>
<b>2</b>	<b>THEORY FRAMEWORK</b>	<b>3</b>
2.1	The tight-binding method . . . . .	3
2.2	Crystal structure of TMDs . . . . .	5
2.3	Landau level in magnetic field . . . . .	6
2.4	Hall effect . . . . .	8
2.4.1	The classical Hall effect . . . . .	8
2.4.2	Berry curvature . . . . .	9
2.4.3	The Quantum Hall effect . . . . .	11
<b>3</b>	<b>THREE-BAND TIGHT-BINDING MODEL FOR TMDS</b>	<b>13</b>
3.1	Three-band tight-binding model without magnetic field . . . . .	13
3.2	Three-band tight binding model under a magnetic field . . . . .	18
<b>4</b>	<b>RESULTS AND DISCUSSION</b>	<b>26</b>
4.1	Band structure of MoS <sub>2</sub> at zero magnetic field . . . . .	26
4.2	Hofstadter butterfly of monolayer MoS <sub>2</sub> . . . . .	27
4.3	Landau levels in monolayer MoS <sub>2</sub> . . . . .	30
4.4	Color the Hofstadter butterfly . . . . .	32
4.5	Conclusions . . . . .	36
<b>A</b>	<b>Derivation of anomalous Hall conductivity</b>	<b>38</b>
<b>B</b>	<b>Matrix elements of the TB Hamiltonian without SOC</b>	<b>39</b>
<b>C</b>	<b>Details of the Peierls substitution</b>	<b>45</b>
<b>D</b>	<b>Solving the Diophantine equation</b>	<b>46</b>

## LIST OF FIGURES

2.1	Structure of TMD.	5
2.2	Landau levels.	8
2.3	Longitudinal resistance and Hall resistance plot.	9
2.4	Quantum Hall effect by von Klitzing.	11
3.1	The hexagonal structure with neighbor hoppings.	15
3.2	TMD with eighteen neighbors atom M rewrite with the site index.	21
3.3	Magnetic unit cell for TMD monolayers.	23
3.4	A visualization of super matrix.	25
4.1	Banstructure of NN and TNN monolayer MoS <sub>2</sub> with SOC without magnetic field.	27
4.2	Hofstadter butterfly for TMD.	28
4.3	Hofstadter butterfly of monolayer MoS <sub>2</sub> with SOC in the presence of magnetic field.	29
4.4	Landau levels in Hofstadter butterfly.	31
4.5	Colored points version of Hofstadter butterfly.	34
4.6	Gaps color-coded Hofstadter butterfly for NN case.	35
4.7	Gaps color-coded Hofstadter butterfly for TNN case.	36
B.1	Showcase NN Hofstadter's butterflies of MX <sub>2</sub> monolayers.	42
B.2	Showcase TNN Hofstadter's butterflies of MX <sub>2</sub> monolayers.	44

## LIST OF TABLES

3.1	Coordinates relative of hopping terms. . . . .	15
3.2	Symmetry operators of the $D_{3h}$ point group. . . . .	16
B.1	Fitted parameters NN. . . . .	41
B.2	Fitted parameters TNN. . . . .	43
D.1	Values of Chern numbers. . . . .	46

## LIST OF ABBREVIATIONS

<b>LCAO</b> Linear Combination of Atomic Orbital . . . . .	3
<b>TMD</b> transition metal dichalcogenides . . . . .	1
<b>TB</b> tight-binding . . . . .	14
<b>TBM</b> tight-binding model . . . . .	viii
<b>NN</b> nearest-neighbor . . . . .	14
<b>NNN</b> next nearest-neighbor . . . . .	14
<b>TNN</b> third-nearest-neighbor . . . . .	14
<b>2D</b> two-dimensional . . . . .	1
<b>BZ</b> Brillouin zone . . . . .	26
<b>GGA</b> generalized-gradient approximation . . . . .	28
<b>LDA</b> local-density approximation . . . . .	28
<b>SOC</b> spin orbit coupling . . . . .	18
<b>LL</b> Landau levels . . . . .	7

<b>IQHE</b> integer Quantum Hall effect . . . . .	11
<b>FQHE</b> fractional Quantum Hall effect . . . . .	11
<b>TKNN</b> Thouless-Kohmoto-Nightingale-Nijs . . . . .	32
<b>DOS</b> Density of state . . . . .	35
<b>VB</b> valence band . . . . .	26
<b>CB</b> conduction band . . . . .	26

## Abstract

Hofstadter's butterfly has been studied experimentally for 50 years. It was first discovered by computer scientist Douglas Hofstadter. This thesis explores the electronic phenomena in material systems, particularly focusing on monolayer transition metal dichalcogenides. We begin by studying a minimal three-band tight-binding model (TBM) in order to describe the electronic structure of TMD monolayer. In the presence of an external magnetic field, the calculated band energies show Landau levels at small fields and become fractal-structured at strong fields, which is known as the Hofstadter butterfly. Building on this framework, we further explore related quantum phenomena including Landau levels and quantum Hall effect.

**Keywords:** Tight-binding model, Hofstadter butterfly, Honeycomb lattice, Landau levels, quantum Hall effect, transition metal dichalcogenides.

## Tóm tắt

Phổ năng lượng Hofstadter đã được nghiên cứu thực nghiệm trong suốt 50 năm qua. Hiện tượng này lần đầu tiên được phát hiện bởi nhà khoa học máy tính Douglas Hofstadter. Khóa luận này tập trung nghiên cứu các hiện tượng điện tử trong các hệ vật liệu, đặc biệt là lớp đơn của các hợp chất chuyển tiếp kim loại – dichalcogenide. Trước tiên, chúng tôi khảo sát một mô hình ba dải tối giản theo phương pháp liên kết chặt nhằm mô tả cấu trúc điện tử của đơn lớp TMDC. Khi đặt vào một từ trường ngoài, các mức năng lượng được tính toán thể hiện sự hình thành của các mức Landau ở cường độ từ trường yếu và xuất hiện cấu trúc fractal đặc trưng khi từ trường mạnh – hiện tượng được gọi là *Hofstadter butterfly*. Dựa trên mô hình này, chúng tôi tiếp tục khảo sát các hiện tượng lượng tử có liên quan như các mức Landau và hiệu ứng Hall lượng tử.

# CHAPTER 1

## INTRODUCTION

Since the isolation of graphene in 2004, research on the field of two-dimensional (2D) materials has noticeably grown into a major branch of physical science with a wide range of applications. Their unique 2D structure offers an open canvas to tailor and functionalize through layer number, defects, morphology, moiré patterns, strain, and other tunable properties. 2D materials, such as graphene and monolayer transition metal dichalcogenides (TMD), have become a focal point in condensed matter physics due to their extraordinary electronic properties. Over the years, researchers have focused on graphene, with hope that its potential to replace silicon, enabling the continuation of Moore's law in next-generation semiconductor devices. However, in recent years, owing to their potentials, the number of scholarly papers researching graphene's use was enormous, reached a peak of thousand publications annually in 2021. Meanwhile, TMD have created tremendous interest among materials scientists, on account of their huge potential for new types of electronics, optoelectronics and superconductivity. Atomically thin 2D TMD have led to a variety of promising technologies for nanoelectronic, sensing and optoelectronics. Unlike graphene, many 2D TMD are naturally semiconductors and enormously posses potential to be made into ultra-small and low power transistors than silicon. These materials consist of large atom from the transition metal elements that lies in the middle of the periodic table are sandwiched by two layers of atoms from the chalcogenide elements, such as sulfur or selenium, forming a three-layer sandwich called a transition metal dichalcogenides.

Another majority opportunity is unraveling the fundamental behind the unique properties of 2D materials. These systems exhibit a various interesting quantum effects, such as superconductivity, weak localization, topological insulation, and others. In some cases, these quantum effects can lead to novel applications, such as valleytronics or twistronics.

The Hofstadter butterfly have been studied for nearly 50 years with various ranging reportedly from 2D symmetry lattice such as square lattice, triangular lattice, honeycomb

lattice, Kagome lattice to Lieb’s lattice, Mielke’s lattice, Tasaki’s lattice under an uniform magnetic field. The first Hofstadter butterfly was originally made for an electron moving in a 2D square lattice by computer scientist Douglas Hofstadter. The behaviour of an electron in such a quantum system could produce an energy spectrum which leads to a self-similar recursive Landau level spectrum resembling butterfly wings. The idea behind Hofstadter’s butterfly is that you’re looking at how the band structure of electrons moves when you have the magnetic field on one axis and the electrons’ energies on the other, and plotted on that diagram, the band forms a fractal structure that looks like a butterfly.

This thesis is mainly organized to explore the electronic structure of 2D material systems under external magnetic fields, with a particular focus on monolayer TMD.

We begin in Chapter 2 by presenting the theoretical background, including the tight-binding model, the crystal structure of TMDs, Landau quantization, and the Hall effect.

In Chapter 3, we study the three-band tight-binding model introduced in Ref. [1], and then extend it by incorporating the effects of an external magnetic field.

Chapter 4 presents the results obtained from the model developed in Chapter 3. A portion of these results has been previously reported by other research groups Refs. [2, 3], but we also include new findings and a more general approach that broadens the scope of the original model. A key novelty of this work lies in the integration of theoretical elements from Chapter 2, such as Hall effects. To the best of our knowledge, such an explicit incorporation has not been addressed in the existing literature. This theoretical refinement enables a more systematic and physically grounded analysis of the Hofstadter spectrum in monolayer TMDs.

# CHAPTER 2

## THEORY FRAMEWORK

In this chapter, we present the theoretical background underpinning the study, commencing with an introduction to the tight-binding method as the main approach to describe the electronic structure of TMDs. The crystal structure of TMDs is also discussed to determine their symmetries. Additionally, in the presence of a magnetic field, electronic motion becomes quantized into Landau levels, as first proposed by Lev Landau. Following this, we also present the theoretical framework of the Hall effect, beginning with the classical Hall effect and culminating with the quantum Hall effect, as presented in Ref. [4]. The study of Hall effect based largely on the treatment in Ref. [5].

### 2.1 The tight-binding method

The tight-binding approximation is based on the Linear Combination of Atomic Orbital (LCAO) method. This approach constructs electronic wave functions using the atomic orbitals of isolated atoms. In the tight-binding method, we assume the electrons stay close to the atomic sites and the overlap between neighboring orbitals is small. We start with the single electron time-independent Schrödinger equation

$$H_{1e}\psi = \left[ -\frac{\hbar^2 \nabla^2}{2m} + U_0(\mathbf{r}) \right] \psi_{\lambda,\mathbf{k}}(\mathbf{r}) = \varepsilon_{\lambda}(\mathbf{k}) \psi_{\lambda,\mathbf{k}}(\mathbf{r}), \quad (2.1)$$

where  $U_0(\mathbf{r})$  is the periodic lattice potential,  $\psi_{\lambda,\mathbf{k}}(\mathbf{r})$  is the Bloch wavefunction of an electron in band  $\lambda$  with wave vector  $\mathbf{k}$  and  $\varepsilon_{\lambda}(\mathbf{k})$  is the energy dispersion in crystal. In the LCAO method, the electronic wave function can be written as

$$\psi_{\text{LCAO}} = \frac{1}{\sqrt{N}} \sum_{n=1}^N \sum_{i=1}^{N_i} \sum_{j=1}^{N_{\text{orb}}} c_{j,i}(\mathbf{R}_n) \phi_j(\mathbf{r} - \mathbf{R}_n - \mathbf{r}_i), \quad (2.2)$$

in which  $\phi_j$  is the orbital wave function  $j$  of an atomic  $i$  localized on a lattice site  $\mathbf{R}_n$ . Here,  $N_{\text{orb}}$  is the number of orbitals per atom,  $N_i$  is the number of atoms in the unit cell, and  $N$  is the number of unit cells.

As for the tight-binding model (TBM) and the LCAO theory, the single electron Bloch wave function can be expressed in terms of atomic orbitals as follows

$$\psi_{\lambda,\mathbf{k}}(\mathbf{r}) = \frac{1}{\sqrt{N}} \sum_{n=1}^N \sum_{i=1}^{N_i} \sum_{j=1}^{N_{\text{orb}}} C_{j,i}^{\lambda}(\mathbf{k}) e^{i\mathbf{k}\cdot(\mathbf{R}_n+\mathbf{r}_i)} \phi_j(\mathbf{r} - \mathbf{R}_n - \mathbf{r}_i), \quad (2.3)$$

here,  $C_{ji}^{\lambda}(\mathbf{k})$  are the coefficients of linear expansion.

Thanks to the wave function found in Eq. (2.2), now we apply  $e^{-i\mathbf{k}\cdot\mathbf{r}_{i'}} \phi_{j'}^*(\mathbf{r} - \mathbf{r}_{i'})$  to the left of the single electron Schrödinger Eq. (2.1) and taking the sum over  $\mathbf{r}$

$$\sum_{i=1}^{N_i} \sum_{j=1}^{N_{\text{orb}}} (H_{j'i',ji}(\mathbf{k}) - \varepsilon(\mathbf{k}) S_{j'i',ji}(\mathbf{k})) C_{j,i}^{\lambda}(\mathbf{k}) = 0, \quad (2.4)$$

where

$$H_{j,i,ji}(\mathbf{k}) = \int \phi_j^*(\mathbf{r} - \mathbf{r}_i) H_{1e} \phi_j(\mathbf{r} - \mathbf{r}_i), \quad (2.5)$$

is the on-site energy,

$$H_{j'i',ji}(\mathbf{k}) = \sum_{n=1}^N e^{i\mathbf{k}\cdot(\mathbf{R}_n+\mathbf{r}_i-\mathbf{r}_{i'})} \int \phi_{j'}^*(\mathbf{r} - \mathbf{r}_{i'}) H_{1e} \phi_j(\mathbf{r} - \mathbf{R}_n - \mathbf{r}_i), \quad (2.6)$$

is the hopping energy,

$$S_{j'i',ji}(\mathbf{k}) = \sum_{n=1}^N e^{i\mathbf{k}\cdot(\mathbf{R}_n+\mathbf{r}_i-\mathbf{r}_{i'})} \int \phi_{j'}^*(\mathbf{r} - \mathbf{r}_{i'}) \phi_j(\mathbf{r} - \mathbf{R}_n - \mathbf{r}_i), \quad (2.7)$$

is the overlap integral. The terms  $H_{j'i',ji}$  and  $H_{j,i,ji}$  are called the Hamiltonian matrix elements. The solution of the Eq. (2.4) is the eigenvalue  $\varepsilon$  of the Schrödinger Eq. (2.1). Each eigenvalue give an energy dispersion of the system, called the energy band.

The term in Eq. (2.6) is often referred to as the *hopping parameter*, which characterizes the strength of the interaction between atoms at positions  $i$  and  $i'$ . A larger value implies stronger bonding and easier electron transfer between the atoms. In tight-binding theory, these matrix elements are often obtained from experimental data and treated as semi-empirical parameters.

## 2.2 Crystal structure of TMDs

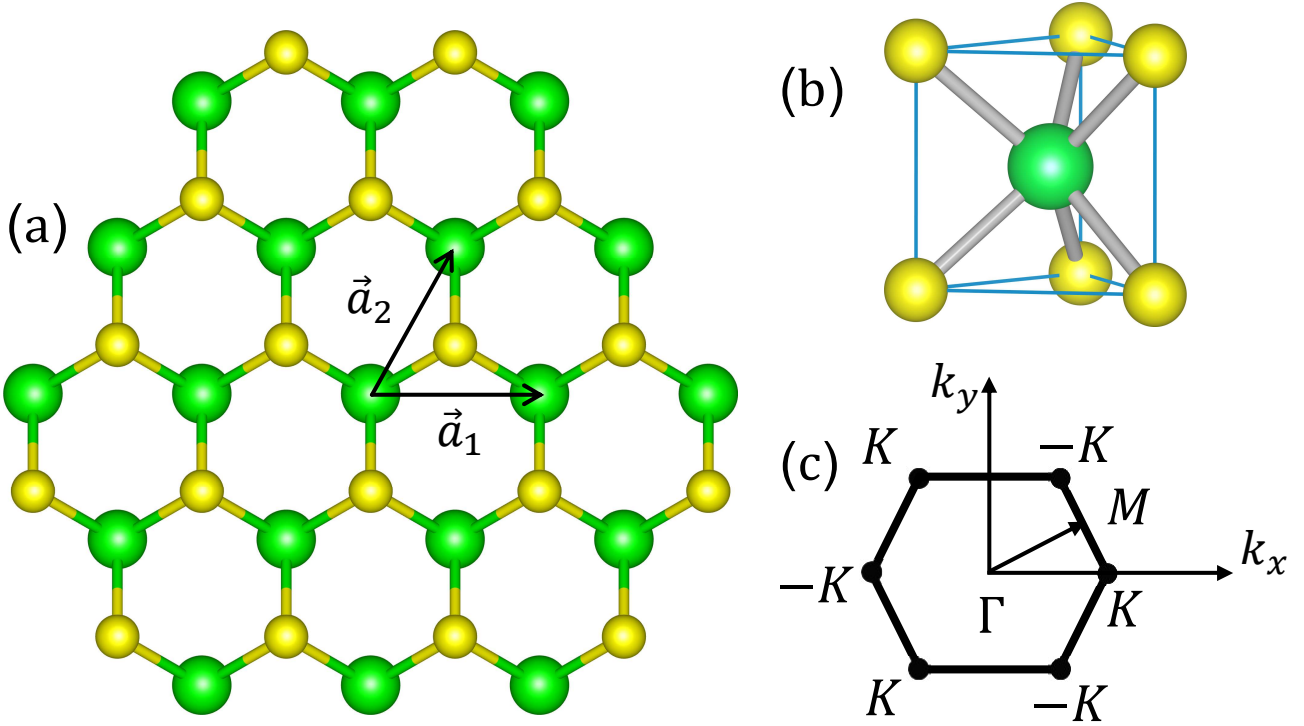


Figure 2.1: Structure of TMD. (a) Top view of monolayer MX<sub>2</sub>. (b) sideview of monolayer MX<sub>2</sub>. The green spheres represent M atoms, which are sandwiched by two layer of X atoms (yellow spheres). (c) The first Brillouin zone and high symmetry points in  $k$ -space.

Monolayer TMDs are 2D materials composed of transition metal and chalcogen atoms arranged in a honeycomb lattice, as illustrated in Fig. 2.1. These materials exhibit  $D_{3h}$  point group symmetry [6]. It were first studied in their buld forms as early as the 1960s, mainly in the context of solid-state and materials science. However, scientists moved their interested in monolayer TMDs, i.e, their 2D form, began to grow significantly after the isolation of graphene in 2004.

In monolayer TMDs, each transition metal (M) atom contributes five  $d$ -orbitals:  $d_{z^2}$ ,  $d_{x^2-y^2}$ ,  $d_{xy}$ ,  $d_{xz}$ , and  $d_{yz}$ , while each chalcogen (X) atom contributes three  $p$ -orbitals:  $p_x$ ,  $p_y$ , and  $p_z$ . The transition metal atoms form a triangular lattice and are sandwiched between two layers of chalcogen atoms, which themselves are arranged on a triangular lattice at alternating hollow sites. This arrangement results in a trigonal prismatic coordination, where each metal atom is surrounded by six chalcogen atoms positioned at the vertices of a trigonal prism, as shown in Fig. 2.1(b). The top view of monolayer

TMDs is shown in Fig. 2.1(a). The Bravais lattice is spanned by the basis vectors

$$\vec{a}_1 = (a, 0, 0), \vec{a}_2 = \left( \frac{a}{2}, \frac{\sqrt{3}}{2}a, 0 \right), \quad (2.8)$$

where  $a$  is lattice constant. The first Brillouin zone of the TMD is hexagonal with the high-symmetry points are defined as follows:  $\Gamma = (0, 0)$ ,  $K = (\frac{4\pi}{3a}, 0)$  and  $M = (\frac{\pi}{a}, \frac{\pi}{\sqrt{3}a})$ .

## 2.3 Landau level in magnetic field

The concept of Landau levels was first introduced by Lev Landau in 1930, describing the quantization of electronic motion in a two-dimensional electron gas under a perpendicular magnetic field. In this section, we briefly revisit the derivation of the Landau level spectrum from the single-particle Hamiltonian, providing a general theoretical overview that lays the foundation for the more complex tight-binding calculations presented later in this thesis.

We begin with the single particle Hamiltonian

$$H = \frac{\mathbf{p}^2}{2m}, \quad (2.9)$$

where we apply the substitution

$$\mathbf{p} \rightarrow \mathbf{p} = \boldsymbol{\Pi} + e\mathbf{A}(\mathbf{r}), \quad (2.10)$$

with  $\mathbf{A}(\mathbf{r})$  specified in the Landau gauge as  $\mathbf{A} = (0, Bx, 0)$ . The Hamiltonian then becomes

$$\begin{aligned} H &= \frac{1}{2m} (\boldsymbol{\Pi} + e\mathbf{A}(\mathbf{r}))^2 \\ &= \frac{\Pi_x^2}{2m} + \frac{(\Pi_y + eBx)^2}{2m}. \end{aligned} \quad (2.11)$$

To diagonalize this Hamiltonian, we define the following ladder operators

$$\begin{aligned} a &= \sqrt{\frac{1}{2\hbar eB}} (\Pi_x + i\Pi_y), \\ a^\dagger &= \sqrt{\frac{1}{2\hbar eB}} (\Pi_x - i\Pi_y), \\ b &= \sqrt{\frac{eB}{2\hbar}} \left( y - \frac{1}{eB} \Pi_x + ix \right), \\ b^\dagger &= \sqrt{\frac{eB}{2\hbar}} \left( y - \frac{1}{eB} \Pi_x - ix \right). \end{aligned} \quad (2.12)$$

The inverse transformations read

$$\begin{aligned}\Pi_x &= \sqrt{\frac{\hbar e B}{2}}(a + a^\dagger), \\ \Pi_y &= i\sqrt{\frac{\hbar e B}{2}}(a^\dagger - a).\end{aligned}\tag{2.13}$$

The operators  $a$  and  $a^\dagger$  satisfy the bosonic commutation relation

$$[a, a^\dagger] = 1, \quad [a, a] = [a^\dagger, a^\dagger] = 0.\tag{2.14}$$

Operators  $b$  and  $b^\dagger$  also obey:

$$[b, b^\dagger] = 1, \quad [b, b] = [b^\dagger, b^\dagger] = 0,\tag{2.15}$$

and in addition, the  $a$  and  $b$  sectors commute:

$$[a, b] = [a, b^\dagger] = [a^\dagger, b] = [a^\dagger, b^\dagger] = 0.\tag{2.16}$$

As in the one-dimensional harmonic oscillator, the ladder operators act as

$$a |n\rangle = \sqrt{n} |n-1\rangle, \quad a^\dagger |n\rangle = \sqrt{n+1} |n+1\rangle,\tag{2.17}$$

where  $|n\rangle$  is an eigenstate of the number operator  $a^\dagger a$  with eigenvalue  $n \geq 0$ .

The Hamiltonian in Eq. (2.11) can now be written in terms of  $a$  and  $a^\dagger$  as

$$H = \hbar\omega_c \left( a^\dagger a + \frac{1}{2} \right), \quad \text{with } \omega_c = \frac{eB}{m}.\tag{2.18}$$

The eigenvalues of Eq. (2.18) are known as Landau levelss (LLs)

$$E_n = (n + 1/2) \hbar\omega_c,\tag{2.19}$$

where  $n$  is the Landau level index and  $\omega_c$  is called the cyclotron frequency. These quantized energy are known as LLs. Each level labeled by the index  $n$ . The Fig. 2.2 illustrates the Landau level energy spectrum as a function of magnetic field strength. Each line represents a discrete energy level labeled by the Landau index  $n$ . As the magnetic field  $B$  increases, the spacing between adjacent grows linearly due to the dependence of the cyclotron frequency  $\omega_c$ . At zero field, the spectrum is continous, corresponding to the free electron case. However, in the presence of magnetic field, the energy is quantized into discrete levels, leading to the characteristic ladder-like structure

shown in the figure.

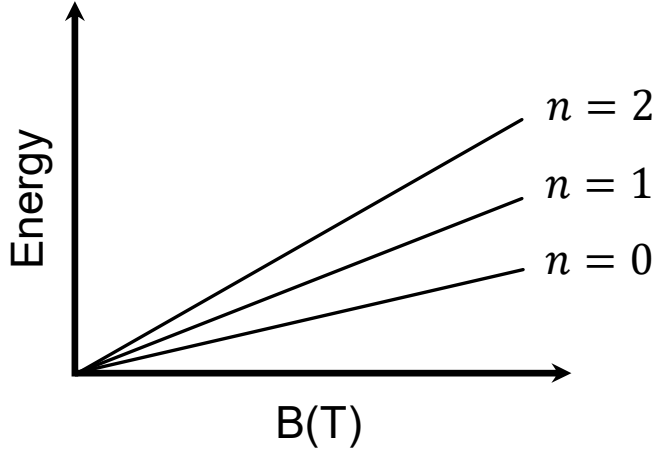


Figure 2.2: Representation of the Landau levels of Eq. 2.19.

## 2.4 Hall effect

### 2.4.1 The classical Hall effect

Before delving into the quantum Hall effect, let us start by taking a look at its classical counterpart i.e., the Hall effect. The Hall effect arises when a conductor carrying an electric current is placed in an external magnetic field  $\mathbf{B}$ . The Lorentz force from the magnetic field causes the charges to accumulate on one side of the conductor. Starting with an electric field  $\mathbf{E}$  established in the solid results in a current density  $\mathbf{J}$  linearly related to the field through Ohm's law

$$\mathbf{J} = \boldsymbol{\sigma} \mathbf{E}, \quad (2.20)$$

$$\mathbf{E} = \sigma^{-1} \mathbf{J} = \rho \mathbf{J}, \quad (2.21)$$

where  $\boldsymbol{\sigma}$  is the conductivity tensor and the resistivity  $\rho$  is defined as the inverse of the conductivity. This remains true when both are tensors

$$\begin{pmatrix} J_x \\ J_y \end{pmatrix} = \begin{pmatrix} \sigma_{xx} & \sigma_{xy} \\ \sigma_{yx} & \sigma_{yy} \end{pmatrix} \begin{pmatrix} E_x \\ E_y \end{pmatrix}, \quad (2.22)$$

$$\begin{pmatrix} E_x \\ E_y \end{pmatrix} \begin{pmatrix} \rho_{xx} & \rho_{xy} \\ \rho_{yx} & \rho_{yy} \end{pmatrix} \begin{pmatrix} J_x \\ J_y \end{pmatrix}. \quad (2.23)$$

The off-diagonal components of resistivity tensor is  $\rho_{xy} = \rho_{yx} = \frac{B}{en}$ . Usually we measure the resistance  $R$ , which differs from the resistivity  $\rho$  by geometric factors. However, for  $\rho_{xy}$ , this thing coincide. To see this, consider a sample of material of length  $L$  in the  $y$ -direction. We drop a voltage  $V_y$  in the  $y$ -direction and measure the resulting current

$I_x$  in the  $x$ -direction. The transverse resistance is

$$R_{xy} = \frac{V_y}{I_x} = \frac{LE_y}{LJ_x} = \frac{E_y}{J_x} = -\rho_{xy}. \quad (2.24)$$

For a current  $I_x$  flowing in the  $x$ -direction, and the corresponded electric field  $E_y$  in the  $y$ -direction, the Hall coefficient is defined by

$$R_H = \frac{\rho_{xy}}{B} = \frac{1}{en}, \quad (2.25)$$

showing the Hall resistance is a constant in the classical regime. We see that the Hall coefficient depends only on microscopic information about the material: the charge and density of conduction particles. The Hall coefficient does not depend on the scattering time  $\tau$ ; it remains unaffected by the specific frictional mechanism present in the material.

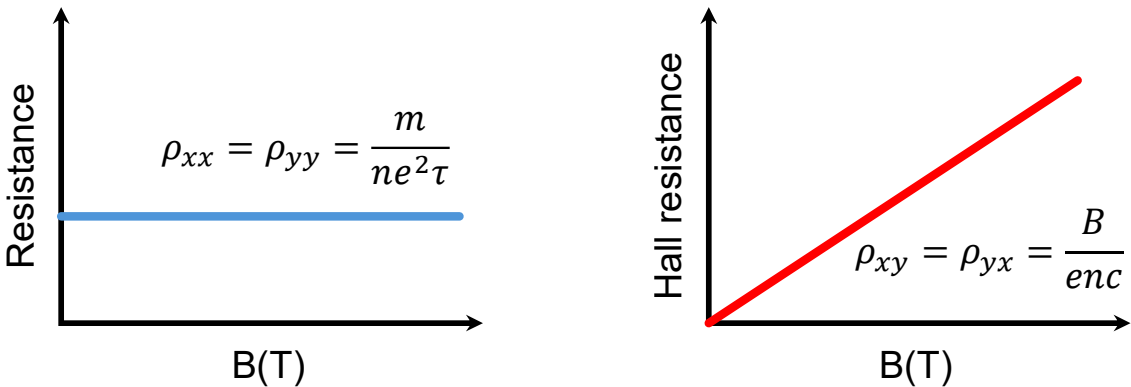


Figure 2.3: The longitudinal resistance on the right figure and the Hall resistance in the left figure. The graph shows both the longitudinal resistance and the Hall resistance is linear to the increasing magnetic field.

## 2.4.2 Berry curvature

While the classical Hall effect is well explained by the Lorentz force deflecting charge carriers under a magnetic field, it fails to capture the quantized nature of Hall conductance observed in two-dimensional electron systems at low temperatures and high magnetic fields. This quantization is inherently quantum mechanical and cannot be described without considering the wavefunction topology of Bloch electrons.

In the semiclassical framework, the motion of electrons in a periodic potential acquires an additional term known as the anomalous velocity, which arises due to the Berry curvature of the Bloch bands. When an external electric field  $\mathbf{E} = (E_x, E_y, 0)$  is applied, the crystal momentum  $\mathbf{k}$  of the Bloch electrons become time-dependent, in

accordance with the semiclassical acceleration theorem

$$\hbar \dot{\mathbf{k}} = -e\mathbf{E}. \quad (2.26)$$

The velocity of Bloch electrons is defined as

$$\mathbf{v}_\nu = \frac{1}{\hbar} \nabla_{\mathbf{k}} \varepsilon_\nu(\mathbf{k}) - \dot{\mathbf{k}} \times \Omega_\nu(\mathbf{k}), \quad (2.27)$$

in which the second term,  $-\dot{\mathbf{k}} \times \Omega_\nu(\mathbf{k})$ , is known as the anomalous velocity. The Berry curvature  $\Omega_\nu(\mathbf{k})$  of the  $\nu$ -th band is given by

$$\Omega_\nu(\mathbf{k}) = \nabla_{\mathbf{k}} \times \Lambda_\nu(\mathbf{k}), \quad (2.28)$$

where the Berry connection is defined as

$$\Lambda_\nu(\mathbf{k}) = i \langle u_{\nu,\mathbf{k}} | \nabla_{\mathbf{k}} u_{\nu,\mathbf{k}} \rangle. \quad (2.29)$$

Substituting Eq. (2.26) into Eq. (2.27), we obtain the velocity for electrons of  $\nu$ -th band

$$\mathbf{v}_\nu(\mathbf{k}) = \frac{1}{\hbar} \nabla_{\mathbf{k}} \varepsilon_\nu(\mathbf{k}) + \frac{e}{\hbar} \mathbf{E} \times \Omega_\nu(\mathbf{k}). \quad (2.30)$$

The electric current density along the  $x$ -direction now is

$$\begin{aligned} J_x &= \frac{1}{L^2} e \langle v_x \rangle \\ &= \frac{e}{\hbar L^2} \sum_{n,\mathbf{k}} \frac{\partial \varepsilon_n(\mathbf{k})}{\partial k_x} f_n(\mathbf{k}) + \frac{e^2}{\hbar L^2} E_y \sum_{n,\mathbf{k}} \Omega_\nu^z(\mathbf{k}) f_n(\mathbf{k}). \end{aligned} \quad (2.31)$$

Eq. (2.31) allows us to express the Hall conductivity in terms of the Berry curvature integrated over all occupied states. This expression also implies that, if no subbands are occupied, the longitudinal conductivity vanishes, i.e.,  $\sigma_{xx} = 0$

$$\sigma_{xy} = \frac{e^2}{h} \sum_n^{\text{occ.}} \frac{1}{2\pi} \iint_{\text{BZ}} dk_x dk_y \Omega_\nu^z(\mathbf{k}). \quad (2.32)$$

The details derivation is given in Appendix A.

### 2.4.3 The Quantum Hall effect

In Section 2.4.1, we arrived at the classical Hall resistance, which remains stable under the classical mechanics framework. However, our world is governed not only by classical physics but also by quantum mechanics. Things changes significantly at extremely low temperatures and strong magnetic fields, revealing new quantum phenomena.

There are two related phenomena which are associated to two different quantum Hall effects. These are called the integer Quantum Hall effect (IQHE) and fractional Quantum Hall effect (FQHE). In this study, we mainly focus on the IQHE where the flux number and flux quanta are integers. This phenomenon can be understood without taking into account the Coulomb interaction between electrons, which means we shall continue using the single electron Hamiltonian that we described in Section 2.1. In this section, we first discovered and subsequently understood theoretically the integer quantum Hall effect in the Hofstadter butterfly.

In two dimensional, there is a crucial relationship between the conductivity tensor  $\sigma$  and the resistivity tensor  $\rho$  is given by

$$\begin{bmatrix} \sigma_{xx} & \sigma_{xy} \\ \sigma_{yx} & \sigma_{yy} \end{bmatrix} \begin{bmatrix} \rho_{xx} & \rho_{xy} \\ \rho_{yx} & \rho_{yy} \end{bmatrix}^{-1} = \frac{1}{\rho_{xx}\rho_{yy} - \rho_{xy}\rho_{yx}} \begin{bmatrix} \rho_{yy} & -\rho_{xy} \\ -\rho_{yx} & \rho_{xx} \end{bmatrix}. \quad (2.33)$$

Let's take a look at the experimental data for the quantum Hall effect were performed in 1980 by von Klitzing *et al.* [4]

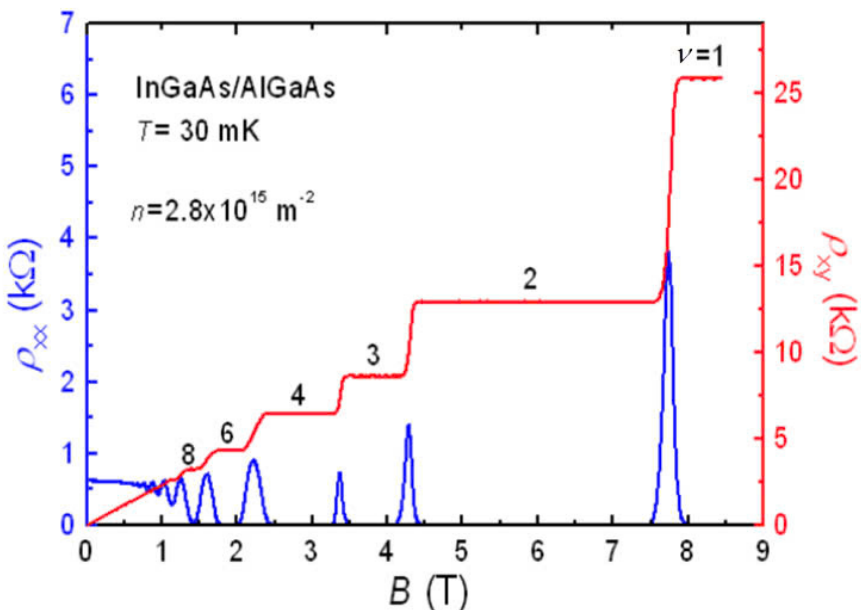


Figure 2.4: This is the integer quantum Hall effect. For this Klaus von Klitzing was awarded the 1985 Nobel prize.

Both the Hall resistivity  $\rho_{xy}$  and the longitudinal resistivity  $\rho_{xx}$  depict fascinating behaviour. Perhaps the most striking feature in the figure is the fact that the Hall resistivity  $\rho_{xy}$  sits on a plateau for a range of magnetic field, before jumping dramatically to the next plateau, while the longitudinal spikes sharply at the transitions between plateaux but vanishes on the plateaux themselves.

The Hall resistivity is now defined

$$\rho_{xy} = \frac{R_K}{\nu}, \quad \nu = 1, 2, \dots \quad (2.34)$$

while  $\nu$  is the total filled Landau levels and  $R_K$  is Klitzing's resistance constant

$$R_K = \frac{h}{e^2} = 25812.8074555\Omega \pm 0.0000059\Omega. \quad (2.35)$$

Between two plateaux, if  $\rho_{xy} = 0$  then we get the familiar relation between resistivity and conductivity is  $\sigma_{xx} = 1/\rho_{xx}$ . But on these Hall plateaux

$$\rho_{xy} = \rho_{yx} = \text{const}, \quad \rho_{xx} = \rho_{yy} = 0, \quad (2.36)$$

this leads to

$$\sigma_{xy} = \sigma_{yx} = 1/\text{const}, \quad \sigma_{xx} = \sigma_{yy} = 0. \quad (2.37)$$

There is an apparent paradox here, we would call a system with  $\rho_{xx} = 0$  is a perfect conductor, while one with  $\sigma_{xx} = 0$  is a perfect insulator. But what if both  $\rho_{xx} = 0$  and  $\sigma_{xx} = 0$  occur simultaneously? A new material or a new state of matter?

## CHAPTER 3

### THREE-BAND TIGHT-BINDING MODEL FOR TMDS

In this chapter, based on the tight-binding framework introduced in Chapter 2, we adopt the model developed by Liu *et al.* [1], which constructs a minimal three-band model using three transition metal orbitals as the basis. This model is commonly referred to as the three-band tight-binding model. Next, we extend this model to include the effects of an external magnetic field by using the Peierls substitution. Finally, we derive the Hamiltonian in the presence of the magnetic field.

### 3.1 Three-band tight-binding model without magnetic field

We take MoS<sub>2</sub> as a representative example and, based on previous *ab initio* calculations, observe that at high-symmetry points in the Brillouin zone, specifically  $\Gamma$ ,  $K$ , and  $M$ , the regions near the highest valence band and lowest conduction band are primarily contributed by the molybdenum  $d_{z^2}$ ,  $d_{xy}$ , and  $d_{x^2-y^2}$  orbitals. In contrast, the  $d_{xz}$ ,  $d_{yz}$  orbitals of molybdenum and the  $p_x$ ,  $p_y$ , and  $p_z$  orbitals of sulfur contribute mainly to higher-energy subbands. This indicates that the low-energy bands near the band gap are predominantly governed by the  $d_{z^2}$ ,  $d_{xy}$ , and  $d_{x^2-y^2}$  orbitals.

Since only the orbitals of the M atom are included, we ignore the sum over atomic positions  $\mathbf{r}_i$  within the unit cell in Eq. (2.3), and denote the wave functions of the three orbitals of the M atom as

$$|\phi_1\rangle = |d_{z^2}\rangle, \quad |\phi_2\rangle = |d_{xy}\rangle, \quad |\phi_3\rangle = |d_{x^2-y^2}\rangle. \quad (3.1)$$

The Bloch wavefunction in this model has the form

$$\psi_{\lambda,\mathbf{k}}(\mathbf{r}) = \sum_{j=1}^3 C_j^\lambda(\mathbf{k}) \sum_{\mathbf{R}} e^{i\mathbf{k}\cdot\mathbf{R}} \phi_j(\mathbf{r} - \mathbf{R}). \quad (3.2)$$

The coefficients  $C_j^\lambda(\mathbf{k})$  are the solutions of the eigenvalue equation

$$\sum_{jj'}^3 \left[ H_{jj'}^{\text{TB}}(\mathbf{k}) - \varepsilon_\lambda(\mathbf{k}) S_{jj'}(\mathbf{k}) \right] C_j^\lambda(\mathbf{k}) = 0, \quad (3.3)$$

where

$$H_{jj'}^{\text{TB}}(\mathbf{k}) = \sum_{\mathbf{R}} e^{i\mathbf{k}\cdot\mathbf{R}} \langle \phi_j(\mathbf{r}) | \left[ -\frac{\hbar^2 \nabla^2}{2m} + U_0(\mathbf{r}) \right] | \phi_{j'}(\mathbf{r} - \mathbf{R}) \rangle, \quad (3.4)$$

and

$$S_{jj'}(\mathbf{k}) = \sum_{\mathbf{R}} \langle \phi_j(\mathbf{r}) | \phi_{j'}(\mathbf{r} - \mathbf{R}) \rangle \approx \delta_{jj'}. \quad (3.5)$$

Take into account up to third-nearest-neighbor (TNN) hopping, the matrix elements of the tight-binding (TB) Hamiltonian Eq. (3.4) are

$$\begin{aligned} H_{jj'}^{\text{TNN}}(\mathbf{k}) = & \mathcal{E}_{jj'}(\mathbf{0}) + e^{i\mathbf{k}\cdot\mathbf{R}_1} \mathcal{E}_{jj'}(\mathbf{R}_1) + e^{i\mathbf{k}\cdot\mathbf{R}_2} \mathcal{E}_{jj'}(\mathbf{R}_2) + e^{i\mathbf{k}\cdot\mathbf{R}_3} \mathcal{E}_{jj'}(\mathbf{R}_3) \\ & + e^{i\mathbf{k}\cdot\mathbf{R}_4} \mathcal{E}_{jj'}(\mathbf{R}_4) + e^{i\mathbf{k}\cdot\mathbf{R}_5} \mathcal{E}_{jj'}(\mathbf{R}_5) + e^{i\mathbf{k}\cdot\mathbf{R}_6} \mathcal{E}_{jj'}(\mathbf{R}_6) \\ & + e^{i\mathbf{k}\cdot\tilde{\mathbf{R}}_1} \mathcal{E}_{jj'}(\tilde{\mathbf{R}}_1) + e^{i\mathbf{k}\cdot\tilde{\mathbf{R}}_2} \mathcal{E}_{jj'}(\tilde{\mathbf{R}}_2) + e^{i\mathbf{k}\cdot\tilde{\mathbf{R}}_3} \mathcal{E}_{jj'}(\tilde{\mathbf{R}}_3) \\ & + e^{i\mathbf{k}\cdot\tilde{\mathbf{R}}_4} \mathcal{E}_{jj'}(\tilde{\mathbf{R}}_4) + e^{i\mathbf{k}\cdot\tilde{\mathbf{R}}_5} \mathcal{E}_{jj'}(\tilde{\mathbf{R}}_5) + e^{i\mathbf{k}\cdot\tilde{\mathbf{R}}_6} \mathcal{E}_{jj'}(\tilde{\mathbf{R}}_6) \\ & + e^{i\mathbf{k}\cdot 2\mathbf{R}_1} \mathcal{E}_{jj'}(2\mathbf{R}_1) + e^{i\mathbf{k}\cdot 2\mathbf{R}_2} \mathcal{E}_{jj'}(2\mathbf{R}_2) + e^{i\mathbf{k}\cdot 2\mathbf{R}_3} \mathcal{E}_{jj'}(2\mathbf{R}_3) \\ & + e^{i\mathbf{k}\cdot 2\mathbf{R}_4} \mathcal{E}_{jj'}(2\mathbf{R}_4) + e^{i\mathbf{k}\cdot 2\mathbf{R}_5} \mathcal{E}_{jj'}(2\mathbf{R}_5) + e^{i\mathbf{k}\cdot 2\mathbf{R}_6} \mathcal{E}_{jj'}(2\mathbf{R}_6), \end{aligned} \quad (3.6)$$

where

$$\mathcal{E}_{jj'}(\mathbf{R}) = \langle \phi_j(\mathbf{r}) | \left[ -\frac{\hbar^2 \nabla^2}{2m} + U_0(\mathbf{r}) \right] | \phi_{j'}(\mathbf{r} - \mathbf{R}) \rangle, \quad (3.7)$$

and  $\mathbf{R}_i$ ,  $\tilde{\mathbf{R}}_i$  and  $2\mathbf{R}_i$  are one of the nearest-neighbor (NN), next nearest-neighbor (NNN) and third-nearest-neighbor (TNN) vectors, respectively, where  $i = 1, \dots, 6$ , see in Fig. 3.1. In Table 3.1, we summarize the coordinates of hopping vectors considered in the model.

Vector	Hopping relative coordinates	Cartesian's coordinates
$\mathbf{R}_1$	$(m, n) \rightarrow (m + 2, n)$	$a(1, 0, 0)$
$\mathbf{R}_2$	$(m, n) \rightarrow (m + 1, n - 1)$	$a\left(\frac{1}{2}, -\frac{\sqrt{3}}{2}, 0\right)$
$\mathbf{R}_3$	$(m, n) \rightarrow (m - 1, n - 1)$	$a\left(-\frac{1}{2}, -\frac{\sqrt{3}}{2}, 0\right)$
$\mathbf{R}_4$	$(m, n) \rightarrow (m - 2, n)$	$a(-1, 0, 0)$
$\mathbf{R}_5$	$(m, n) \rightarrow (m - 1, n + 1)$	$a\left(-\frac{1}{2}, \frac{\sqrt{3}}{2}, 0\right)$
$\mathbf{R}_6$	$(m, n) \rightarrow (m + 1, n + 1)$	$a\left(-\frac{1}{2}, \frac{\sqrt{3}}{2}, 0\right)$
$\tilde{\mathbf{R}}_1$	$(m, n) \rightarrow (m + 3, n - 1)$	$l\left(\frac{\sqrt{3}}{2}, -\frac{1}{2}, 0\right)$
$\tilde{\mathbf{R}}_2$	$(m, n) \rightarrow (m, n - 2)$	$l(0, -1, 0)$
$\tilde{\mathbf{R}}_3$	$(m, n) \rightarrow (m - 3, n - 1)$	$l\left(-\frac{\sqrt{3}}{2}, -\frac{1}{2}, 0\right)$
$\tilde{\mathbf{R}}_4$	$(m, n) \rightarrow (m - 3, n + 1)$	$l\left(-\frac{\sqrt{3}}{2}, \frac{1}{2}, 0\right)$
$\tilde{\mathbf{R}}_5$	$(m, n) \rightarrow (m, n + 2)$	$l(0, -1, 0)$
$\tilde{\mathbf{R}}_6$	$(m, n) \rightarrow (m + 3, n + 1)$	$l\left(\frac{\sqrt{3}}{2}, \frac{1}{2}, 0\right)$
$2\mathbf{R}_1$	$(m, n) \rightarrow (m + 4, n)$	$a(2, 0, 0)$
$2\mathbf{R}_2$	$(m, n) \rightarrow (m + 2, n - 2)$	$a(1, -\sqrt{3}, 0)$
$2\mathbf{R}_3$	$(m, n) \rightarrow (m - 2, n - 2)$	$a(-1, -\sqrt{3}, 0)$
$2\mathbf{R}_4$	$(m, n) \rightarrow (m - 4, n)$	$a(-2, 0, 0)$
$2\mathbf{R}_5$	$(m, n) \rightarrow (m - 2, n + 2)$	$a(-1, \sqrt{3}, 0)$
$2\mathbf{R}_6$	$(m, n) \rightarrow (m + 2, n + 2)$	$a(1, \sqrt{3}, 0)$

Table 3.1: Hopping vectors used in the model and their hopping respective relative coordinates to the original site  $(m, n)$ , where  $a = 3.190 \text{ \AA}$  is lattice constant and  $l = a\sqrt{3}$ .

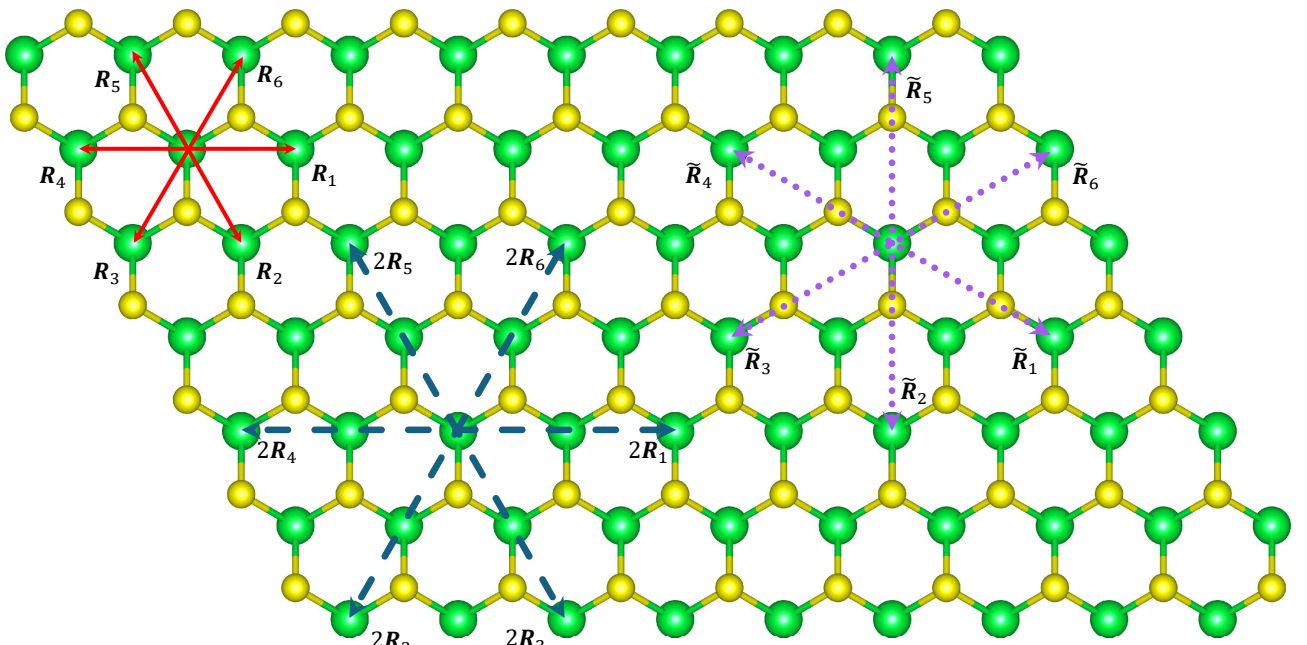


Figure 3.1: The hexagonal structure of the monolayer TMD with the metal atoms at the green larger circles and the chalcogen atoms at the smaller yellow circles. The solid red, dash blue and dot purple arrows prerepresent<sup>15</sup>the NN ( $\mathbf{R}_i$ ), NNN ( $\tilde{\mathbf{R}}_i$ ) and TNN ( $2\mathbf{R}_i$ ), respectively, and  $\mathbf{R}$  are lattice vectors, where  $i = 1, \dots, 6$ .

$g_n$	$x'$	$y'$	$z'$	$z'^2$	$x'y'$	$\frac{1}{2}(x'^2 - y'^2)$
$E$	$x$	$y$	$z$	$z^2$	$xy$	$\frac{1}{2}(x^2 - y^2)$
$C_3(\frac{-2\pi}{3})$	$-\frac{1}{2}x + \frac{\sqrt{3}}{2}y$	$-\frac{\sqrt{3}}{2}x - \frac{1}{2}y$	$z$	$z^2$	$-\frac{1}{2}xy + \frac{\sqrt{3}}{4}(x^2 + y^2)$	$-\frac{\sqrt{3}}{2}xy - \frac{1}{4}(x^2 - y^2)$
$C_3(\frac{-4\pi}{3})$	$-\frac{1}{2}x - \frac{\sqrt{3}}{2}y$	$\frac{\sqrt{3}}{2}x + \frac{1}{2}y$	$z$	$z^2$	$-\frac{1}{2}xy - \frac{\sqrt{3}}{4}(x^2 + y^2)$	$\frac{\sqrt{3}}{2}xy - \frac{1}{4}(x^2 - y^2)$
$C_2(-\pi)$	$-x$	$-y$	$z$	$z^2$	$xy$	$\frac{1}{2}(x^2 - y^2)$
$\sigma_\nu$	$-x$	$y$	$z$	$z^2$	$-xy$	$\frac{1}{2}(x^2 - y^2)$
$\sigma'_\nu$	$\frac{1}{2}x - \frac{\sqrt{3}}{2}$	$-\frac{\sqrt{3}}{2}x - \frac{1}{2}y$	$z$	$z^2$	$\frac{1}{2}xy - \frac{\sqrt{3}}{4}(x^2 + y^2)$	$-\frac{\sqrt{3}}{2}xy - \frac{1}{4}(x^2 - y^2)$
$\sigma''_\nu$	$\frac{1}{2}x + \frac{\sqrt{3}}{2}$	$\frac{\sqrt{3}}{2}x - \frac{1}{2}y$	$z$	$z^2$	$\frac{1}{2}xy + \frac{\sqrt{3}}{4}(x^2 + y^2)$	$\frac{\sqrt{3}}{2}xy - \frac{1}{4}(x^2 - y^2)$

Table 3.2: Some symmetry operators of the  $D_{3h}$  point group on basis functions taking  $(x, y, z)$  into  $(x', y', z')$ .  $C_3(\frac{-2\pi}{3})$  and  $C_3(\frac{-4\pi}{3})$  are the rotations by  $\frac{-2\pi}{3}$  and  $\frac{-4\pi}{3}$  around the  $z$  axis, respectively.  $\sigma_\nu$  is the reflection angular bisector of  $R_1$  and  $R_6$  in Fig. 2.1, and  $\sigma'_\nu, \sigma''_\nu$  are obtained through rotating  $\sigma_\nu$  around the  $z$  axis by  $2\pi/3$  and  $4\pi/3$ , respectively.

One parameterizes the matrices  $\mathcal{E}(\mathbf{0}), \mathcal{E}(\mathbf{R}_1), \mathcal{E}(\tilde{\mathbf{R}}_1), \mathcal{E}(\tilde{\mathbf{R}}_4)$  and  $\mathcal{E}(2\mathbf{R}_1)$  by

$$\begin{aligned} \mathcal{E}(\mathbf{0}) &= \begin{pmatrix} \epsilon_1 & 0 & 0 \\ 0 & \epsilon_2 & 0 \\ 0 & 0 & \epsilon_2 \end{pmatrix}, \mathcal{E}(\mathbf{R}_1) = \begin{pmatrix} t_0 & t_1 & t_2 \\ -t_1 & t_{11} & t_{12} \\ t_2 & -t_{12} & t_{22} \end{pmatrix}, \mathcal{E}(2\mathbf{R}_1) = \begin{pmatrix} u_0 & u_1 & u_2 \\ -u_1 & u_{11} & u_{12} \\ u_2 & -u_{12} & u_{22} \end{pmatrix}, \\ \mathcal{E}(\tilde{\mathbf{R}}_1) &= \begin{pmatrix} r_0 & r_1 & -\frac{r_1}{\sqrt{3}} \\ r_2 & r_{11} & r_{12} \\ -\frac{r_2}{\sqrt{3}} & r_{12} & r_{11} + \frac{2\sqrt{3}}{3}r_{12} \end{pmatrix}, \mathcal{E}(\tilde{\mathbf{R}}_4) = \mathcal{E}(\tilde{\mathbf{R}}_1)^T = \begin{pmatrix} r_0 & r_2 & -\frac{r_2}{\sqrt{3}} \\ r_1 & r_{11} & r_{12} \\ -\frac{r_1}{\sqrt{3}} & r_{12} & r_{11} + \frac{2\sqrt{3}}{3}r_{12} \end{pmatrix}. \end{aligned} \quad (3.8)$$

Given  $\mathcal{E}(\mathbf{R}_1), \mathcal{E}(2\mathbf{R}_1), \mathcal{E}(\tilde{\mathbf{R}}_1), \mathcal{E}(\tilde{\mathbf{R}}_4)$ , the matrix  $\mathcal{E}(\mathbf{R}_i)$  corresponding to all neighbor sites  $\mathbf{R}_i$  can be generated by

$$\mathcal{E}(g_n \mathbf{R}) = D(g_n) \mathcal{E}(\mathbf{R}) D^\dagger(g_n), \quad (3.9)$$

where  $D(g_n)$  is the matrix of the irreducible representation,  $g_n$  are symmetry operators of  $D_{3h}$  point groups,  $\{E, 2C_3, 3C_2, 2S_3, \sigma_h, 3\sigma_\nu\}$ , see in Appendix B for more details about the calculation. Table 2.2 depicts the transformation of the basis functions under the action of symmetry operators. Also, from Table 3.2, we obtain irreducible matrices

as follows

$$\begin{aligned}
D(C_3(-\frac{2\pi}{3})) &= \begin{pmatrix} 1 & 0 & 0 \\ 0 & -1/2 & \sqrt{3}/2 \\ 0 & -\sqrt{3}/2 & -1/2 \end{pmatrix}, \quad D(C_3(-\frac{4\pi}{3})) = \begin{pmatrix} 1 & 0 & 0 \\ 0 & -1/2 & -\sqrt{3}/2 \\ 0 & \sqrt{3}/2 & -1/2 \end{pmatrix}, \\
D(\sigma_\nu) &= \begin{pmatrix} 1 & 0 & 0 \\ 0 & -1 & 0 \\ 0 & 0 & 1 \end{pmatrix}, \quad D(\sigma'_\nu) = \begin{pmatrix} 1 & 0 & 0 \\ 0 & 1/2 & -\sqrt{3}/2 \\ 0 & -\sqrt{3}/2 & -1/2 \end{pmatrix}, \\
D(\sigma''_\nu) &= \begin{pmatrix} 1 & 0 & 0 \\ 0 & 1/2 & \sqrt{3}/2 \\ 0 & \sqrt{3}/2 & -1/2 \end{pmatrix}.
\end{aligned} \tag{3.10}$$

The remaining hopping matrices can be obtained by applying the  $C_3$  rotation, mirror, and relation  $\mathcal{E}(-\mathbf{R}) = \mathcal{E}(\mathbf{R})^T$ . Therefore, we have the hopping terms for three-band TBM including TNN are given in Appendix B.

The TNN tight-binding Hamiltonian now can be written as

$$H^{\text{TNN}}(\mathbf{k}) = \begin{pmatrix} V_0 & V_1 & V_2 \\ V_1^* & V_{11} & V_{12} \\ V_2^* & V_{12}^* & V_{22} \end{pmatrix}, \tag{3.11}$$

where

$$\begin{aligned}
V_0 &= \epsilon_1 + 2t_0(2 \cos \alpha \cos \beta + \cos 2\alpha) + 2r_0(2 \cos 3\alpha \cos \beta + \cos 2\beta), \\
\text{Re}[V_1] &= -2\sqrt{3}t_2 \sin \alpha \sin \beta + 2(r_1 + r_2) \sin 3\alpha \sin \beta - 2\sqrt{3}u_2 \sin 2\alpha \sin 2\beta, \\
\text{Im}[V_1] &= 2t_1 \sin \alpha(2 \cos \alpha + \cos \beta) + 2(r_1 - r_2) \sin 3\alpha \cos \beta + 2u_1 \sin 2\alpha(2 \cos 2\alpha + \cos 2\beta) \\
\text{Re}[V_2] &= 2t_2(\cos 2\alpha - \cos \alpha \cos \beta) - \frac{2}{\sqrt{3}}(r_1 + r_2)(\cos 3\alpha \cos \beta - \cos 2\beta) \\
&\quad + 2u_2(\cos 4\alpha - \cos 2\alpha \cos 2\beta), \\
\text{Im}[V_2] &= 2\sqrt{3}t_1 \cos \alpha \sin \beta + \frac{2}{\sqrt{3}} \sin \beta(r_1 - r_2)(\cos 3\alpha + 2 \cos \beta), \\
V_{11} &= \epsilon_2 + (t_{11} + 3t_{22}) \cos \alpha \cos \beta + 2t_{11} \cos 2\alpha + 4r_{11} \cos 3\alpha \cos \beta \\
&\quad + 2(r_{11} + \sqrt{3}r_{12}) \cos 2\beta + (u_{11} + 3u_{22}) \cos 2\alpha \cos 2\beta + 2u_{11} \cos 4\alpha, \\
\text{Re}[V_{12}] &= \sqrt{3}(t_{22} - t_{11}) \sin \alpha \sin \beta + 4r_{12} \sin 3\alpha \sin \beta + \sqrt{3}(u_{22} - u_{11}) \sin 2\alpha \sin 2\beta, \\
\text{Im}[V_{12}] &= 4t_{12} \sin \alpha(\cos \alpha - \cos \beta) + 4u_{12} \sin 2\alpha(\cos 2\alpha - \cos 2\beta), \\
V_{22} &= \epsilon_2 + (3t_{11} + t_{22}) \cos \alpha \cos \beta + 2t_{22} \cos 2\alpha + 2r_{11}(2 \cos 3\alpha \cos \beta + \cos 2\beta) \\
&\quad + \frac{2}{\sqrt{3}}r_{12}(4 \cos 3\alpha \cos \beta - \cos 2\beta) + (3u_{11} + u_{22}) \cos 2\alpha \cos 2\beta + 2u_{22} \cos 4\alpha,
\end{aligned} \tag{3.12}$$

$$(\alpha, \beta) = \left( \frac{1}{2}k_x a, \frac{\sqrt{3}}{2}k_y a \right). \quad (3.13)$$

The nineteen tight-binding parameters shown in Table B.2 are determined by fitting to the band structure obtained from *ab initio* calculations.

Due to the significant mass of the transition-metal atom M, its spin orbit coupling (SOC) can be large. For simplicity, we consider only the on-site contribution, which corresponds to the  $\mathbf{L} \cdot \mathbf{S}$  term originating from the *M* atoms. Using the basis set  $\{|d_{z^2}, \uparrow\rangle, |d_{xy}, \uparrow\rangle, |d_{x^2-y^2}, \uparrow\rangle, |d_{z^2}, \downarrow\rangle, |d_{xy}, \downarrow\rangle, |d_{x^2-y^2}, \downarrow\rangle\}$ , we derive the SOC term in the Hamiltonian as

$$H' = \lambda \mathbf{L} \cdot \mathbf{S} = \frac{\lambda}{2} \begin{pmatrix} L_z & L_x - iL_y \\ L_x + iL_y & -L_z \end{pmatrix}, \quad (3.14)$$

in which

$$L_z = \begin{pmatrix} 0 & 0 & 0 \\ 0 & 0 & 2i \\ 0 & -2i & 0 \end{pmatrix}, \quad (3.15)$$

is the matrix of  $\hat{L}_z$  (*z* component of the orbital angular momentum) in bases of  $d_{z^2}, d_{xy}, d_{x^2-y^2}$  and  $\lambda$  is characterized the strength of the SOC. Noting that, under the three bases, the matrix elements of  $\hat{L}_x$  and  $\hat{L}_y$  are all zeros. Therefore the full TB Hamiltonian for the magnetic unit cell with the SOC as follows

$$\begin{aligned} H_{\text{SOC}}(\mathbf{k}) &= \mathbf{I}_2 \otimes H^{TNN}(\mathbf{k}) + H' \\ &= \begin{pmatrix} H_{3 \times 3}(\mathbf{k}) + \frac{\lambda}{2}L_z & 0 \\ 0 & H_{3 \times 3}(\mathbf{k}) - \frac{\lambda}{2}L_z \end{pmatrix}, \end{aligned} \quad (3.16)$$

in which  $\mathbf{I}_2$  is the  $2 \times 2$  identity matrix.

## 3.2 Three-band tight binding model under a magnetic field

Under an uniform magnetic field given by a vector potential  $\mathbf{A}(\mathbf{r})$  the single electron Hamiltonian changes into

$$H = \frac{(-i\hbar\nabla + e\mathbf{A}(\mathbf{r}))^2}{2m} + U_0(\mathbf{r}) + g^*\mu_B\mathbf{B} \cdot \mathbf{L}, \quad (3.17)$$

where  $\mu_B = \frac{e\hbar}{2m}$  is Bohr magneton,  $g^*$  is an effective Landé g-factor,  $\mathbf{B} = \nabla \times \mathbf{A}$  is the uniform magnetic field, and  $\mathbf{L}$  is the angular momentum. It is possible to add a phase factor to the tight-binding wavefunction

$$\psi_{\lambda,\mathbf{k}}(\mathbf{r}) = \sum_{j=1}^3 C_j^\lambda(\mathbf{k}) \sum_{\mathbf{R}} e^{i\mathbf{k}\cdot\mathbf{R}} e^{\theta_{\mathbf{R}}(\mathbf{r})} \phi_j(\mathbf{r} - \mathbf{R}). \quad (3.18)$$

We now have

$$H_{jj'}(\mathbf{k}) = H_{jj'}^{\text{TB}}(\mathbf{k}) + H_{jj'}^Z(\mathbf{k}), \quad (3.19)$$

where

$$\begin{aligned} H_{jj'}^{\text{TB}}(\mathbf{k}) &= \sum_{\mathbf{R}} \langle \phi_j(\mathbf{r}) | e^{-i\theta_0(\mathbf{r})} \left[ \frac{(-i\hbar\nabla + e\mathbf{A}(\mathbf{r}))^2}{2m} + U_0(\mathbf{r}) \right] e^{i\mathbf{k}\cdot\mathbf{R}} e^{\theta_{\mathbf{R}}(\mathbf{r})} | \phi_{j'}(\mathbf{r} - \mathbf{R}) \rangle \\ &= \sum_{\mathbf{R}} \langle \phi_j(\mathbf{r}) | e^{i(\mathbf{k}\cdot\mathbf{R} + \theta_{\mathbf{R}} - \theta_0)} \left[ \frac{(-i\hbar\nabla + e\mathbf{A} + \hbar\nabla\theta_{\mathbf{R}})^2}{2m} + U_0(\mathbf{r}) \right] | \phi_{j'}(\mathbf{r} - \mathbf{R}) \rangle. \end{aligned} \quad (3.20)$$

Since the Zeeman interaction originates from the coupling between the magnetic field and the orbital angular momentum of electrons localized at atomic sites, it is an on-site effect rather than a hopping term. Therefore, the Hamiltonian Zeeman is approximated by keeping only  $\mathbf{R} = 0$  contribution

$$\begin{aligned} H_{jj'}^Z(\mathbf{k}) &= g^* \mu_B \mathbf{B} \cdot \sum_{\mathbf{R}} \langle \phi_j(\mathbf{r}) | e^{i(\mathbf{k}\cdot\mathbf{R} + \theta_{\mathbf{R}} - \theta_0)} \mathbf{L} | \phi_{j'}(\mathbf{r} - \mathbf{R}) \rangle \\ &\approx g^* \mu_B \mathbf{B} \cdot \sum_{\mathbf{R}} \langle \phi_j(\mathbf{r}) | \mathbf{L} | \phi_{j'}(\mathbf{r}) \rangle. \end{aligned} \quad (3.21)$$

By choosing  $\theta_{\mathbf{R}} = -\frac{e}{\hbar} \int_{\mathbf{R}}^{\mathbf{r}} \mathbf{A}(\mathbf{r}') \cdot d\mathbf{r}'$  as Peierls substitution [7], the Hamiltonian in Eq. (3.20) now reads

$$\begin{aligned} H_{jj'}^{\text{TB}}(\mathbf{k}) &= \sum_{\mathbf{R}} \langle \phi_j(\mathbf{r}) | e^{i\mathbf{k}\cdot\mathbf{R} - \frac{ie}{\hbar} \int_{\mathbf{R}}^{\mathbf{r}} \mathbf{A}(\mathbf{r}') \cdot d\mathbf{r}' + \frac{ie}{\hbar} \int_{\mathbf{0}}^{\mathbf{r}} \mathbf{A}(\mathbf{r}') \cdot d\mathbf{r}'} \left[ -\frac{\hbar^2 \nabla^2}{2m} + U_0(\mathbf{r}) \right] | \phi_{j'}(\mathbf{r} - \mathbf{R}) \rangle \\ &= \sum_{\mathbf{R}} e^{i\mathbf{k}\cdot\mathbf{R}} e^{\frac{ie}{\hbar} \int_{\mathbf{0}}^{\mathbf{R}} \mathbf{A}(\mathbf{r}') \cdot d\mathbf{r}'} \langle \phi_j(\mathbf{r}) | e^{-\frac{ie}{\hbar} \Phi_{\mathbf{R},\mathbf{r},\mathbf{0}}} \left[ -\frac{\hbar^2 \nabla^2}{2m} + U_0(\mathbf{r}) \right] | \phi_{j'}(\mathbf{r} - \mathbf{R}) \rangle, \end{aligned} \quad (3.22)$$

where  $\Phi_{\mathbf{R},\mathbf{r},\mathbf{0}} = \oint_{\mathbf{R},\mathbf{r},\mathbf{0}} \mathbf{A}(\mathbf{r}') \cdot d\mathbf{r}'$  is the closed loop line integral of  $\mathbf{A}$  along the triangle points  $\mathbf{R}, \mathbf{r}, \mathbf{0}$ , and  $\int_{\mathbf{0}}^{\mathbf{R}} \mathbf{A}(\mathbf{r}') \cdot d\mathbf{r}'$  is the path integral along the two points  $\mathbf{R}, \mathbf{0}$ . Besides

that, we have used the fact that

$$\int_{\mathbf{R}}^{\mathbf{r}} \mathbf{A}(\mathbf{r}') \cdot d\mathbf{r}' + \int_{\mathbf{r}}^{\mathbf{0}} \mathbf{A}(\mathbf{r}') \cdot d\mathbf{r}' = \Phi_{\mathbf{R}, \mathbf{r}, \mathbf{0}} - \int_{\mathbf{0}}^{\mathbf{R}} \mathbf{A}(\mathbf{r}') \cdot d\mathbf{r}'. \quad (3.23)$$

We can show that the flux term  $\Phi_{\mathbf{R}, \mathbf{r}, \mathbf{0}}$  is negligibly small based on two observations [8]. Firstly, when  $\mathbf{r}$  is far from the lattice points  $\mathbf{R}$  and  $\mathbf{0}$ , the enclosed flux may be large. However, since the atomic orbitals are highly localized at these two lattice sites, the corresponding hopping amplitude becomes vanishingly small, effectively suppressing the entire hopping term. Second, when  $\mathbf{r}$  is located at or near either of the two lattice points, the triangle formed is small. Under the assumption of a weak magnetic field, the flux term  $\Phi_{\mathbf{R}, \mathbf{r}, \mathbf{0}}$  in this case approaches zero. These considerations give us the Hamiltonian as

$$H_{jj'}^{\text{TB}}(\mathbf{k}) = \sum_{\mathbf{R}} e^{i\mathbf{k} \cdot \mathbf{R}} e^{\frac{ie}{\hbar} \int_0^{\mathbf{R}} \mathbf{A}(\mathbf{r}') \cdot d\mathbf{r}'} \langle \phi_j(\mathbf{r}) | \left[ -\frac{\hbar^2 \nabla^2}{2m} + U_0(\mathbf{r}) \right] | \phi_{j'}(\mathbf{r} - \mathbf{R}) \rangle. \quad (3.24)$$

Considering only NN, NNN, TNN hoppings, Eq. (3.24) becomes

$$\begin{aligned} H_{jj'}^{\text{TB}}(\mathbf{k}) &= \sum_{\mathbf{R}} e^{i\mathbf{k} \cdot \mathbf{R}} e^{\frac{e}{\hbar} \int_0^{\mathbf{R}} A(\mathbf{r}') \cdot d\mathbf{r}'} \mathcal{E}_{jj'}(\mathbf{R}) \\ &= \mathcal{E}_{jj'}(\mathbf{0}) + e^{i\mathbf{k} \cdot \mathbf{R}_1} e^{\frac{e}{\hbar} \int_0^{\mathbf{R}_1} A(\mathbf{r}') \cdot d\mathbf{r}'} \mathcal{E}_{jj'}(\mathbf{R}_1) + e^{i\mathbf{k} \cdot \mathbf{R}_2} e^{\frac{e}{\hbar} \int_0^{\mathbf{R}_2} A(\mathbf{r}') \cdot d\mathbf{r}'} \mathcal{E}_{jj'}(\mathbf{R}_2) \\ &\quad + e^{i\mathbf{k} \cdot \mathbf{R}_3} e^{\frac{e}{\hbar} \int_0^{\mathbf{R}_3} A(\mathbf{r}') \cdot d\mathbf{r}'} \mathcal{E}_{jj'}(\mathbf{R}_3) + e^{i\mathbf{k} \cdot \mathbf{R}_4} e^{\frac{e}{\hbar} \int_0^{\mathbf{R}_4} A(\mathbf{r}') \cdot d\mathbf{r}'} \mathcal{E}_{jj'}(\mathbf{R}_4) \\ &\quad + e^{i\mathbf{k} \cdot \mathbf{R}_5} e^{\frac{e}{\hbar} \int_0^{\mathbf{R}_5} A(\mathbf{r}') \cdot d\mathbf{r}'} \mathcal{E}_{jj'}(\mathbf{R}_5) + e^{i\mathbf{k} \cdot \mathbf{R}_6} e^{\frac{e}{\hbar} \int_0^{\mathbf{R}_6} A(\mathbf{r}') \cdot d\mathbf{r}'} \mathcal{E}_{jj'}(\mathbf{R}_6) \\ &\quad + e^{i\mathbf{k} \cdot \tilde{\mathbf{R}}_1} e^{\frac{e}{\hbar} \int_0^{\tilde{\mathbf{R}}_1} A(\mathbf{r}') \cdot d\mathbf{r}'} \mathcal{E}_{jj'}(\tilde{\mathbf{R}}_1) + e^{i\mathbf{k} \cdot \tilde{\mathbf{R}}_2} e^{\frac{e}{\hbar} \int_0^{\tilde{\mathbf{R}}_2} A(\mathbf{r}') \cdot d\mathbf{r}'} \mathcal{E}_{jj'}(\tilde{\mathbf{R}}_2) \\ &\quad + e^{i\mathbf{k} \cdot \tilde{\mathbf{R}}_3} e^{\frac{e}{\hbar} \int_0^{\tilde{\mathbf{R}}_3} A(\mathbf{r}') \cdot d\mathbf{r}'} \mathcal{E}_{jj'}(\tilde{\mathbf{R}}_3) + e^{i\mathbf{k} \cdot \tilde{\mathbf{R}}_4} e^{\frac{e}{\hbar} \int_0^{\tilde{\mathbf{R}}_4} A(\mathbf{r}') \cdot d\mathbf{r}'} \mathcal{E}_{jj'}(\tilde{\mathbf{R}}_4) \\ &\quad + e^{i\mathbf{k} \cdot \tilde{\mathbf{R}}_5} e^{\frac{e}{\hbar} \int_0^{\tilde{\mathbf{R}}_5} A(\mathbf{r}') \cdot d\mathbf{r}'} \mathcal{E}_{jj'}(\tilde{\mathbf{R}}_5) + e^{i\mathbf{k} \cdot \tilde{\mathbf{R}}_6} e^{\frac{e}{\hbar} \int_0^{\tilde{\mathbf{R}}_6} A(\mathbf{r}') \cdot d\mathbf{r}'} \mathcal{E}_{jj'}(\tilde{\mathbf{R}}_6) \\ &\quad + e^{i\mathbf{k} \cdot \mathbf{R}'_1} e^{\frac{e}{\hbar} \int_0^{\mathbf{R}'_1} A(\mathbf{r}') \cdot d\mathbf{r}'} \mathcal{E}_{jj'}(\mathbf{R}'_1) + e^{i\mathbf{k} \cdot \mathbf{R}'_2} e^{\frac{e}{\hbar} \int_0^{\mathbf{R}'_2} A(\mathbf{r}') \cdot d\mathbf{r}'} \mathcal{E}_{jj'}(\mathbf{R}'_2) \\ &\quad + e^{i\mathbf{k} \cdot \mathbf{R}'_3} e^{\frac{e}{\hbar} \int_0^{\mathbf{R}'_3} A(\mathbf{r}') \cdot d\mathbf{r}'} \mathcal{E}_{jj'}(\mathbf{R}'_3) + e^{i\mathbf{k} \cdot \mathbf{R}'_4} e^{\frac{e}{\hbar} \int_0^{\mathbf{R}'_4} A(\mathbf{r}') \cdot d\mathbf{r}'} \mathcal{E}_{jj'}(\mathbf{R}'_4) \\ &\quad + e^{i\mathbf{k} \cdot \mathbf{R}'_5} e^{\frac{e}{\hbar} \int_0^{\mathbf{R}'_5} A(\mathbf{r}') \cdot d\mathbf{r}'} \mathcal{E}_{jj'}(\mathbf{R}'_5) + e^{i\mathbf{k} \cdot \mathbf{R}'_6} e^{\frac{e}{\hbar} \int_0^{\mathbf{R}'_6} A(\mathbf{r}') \cdot d\mathbf{r}'} \mathcal{E}_{jj'}(\mathbf{R}'_6), \end{aligned} \quad (3.25)$$

where  $\mathbf{R}_i$ ,  $\tilde{\mathbf{R}}_i$  and  $\mathbf{R}'_i = 2\mathbf{R}_i$  are NN, NNN, TNN vectors, with  $i = 1, 2, \dots, 6$ .

In the presence of a perpendicular magnetic field  $\mathbf{B} = (0, 0, B)$  applied to the plane of TMD, we choose the vector potential in the Landau gauge as  $\mathbf{A} = (0, Bx, 0)$ . Suppose that the atom metal M is located at position  $\mathbf{R}_{m,n} = \left(m\frac{a}{2}, n\frac{a\sqrt{3}}{2}\right)$ , where  $m, n \in \mathbb{Z}$ , let

us define a shorthand notation for these extra terms

$$\begin{aligned}\theta_{m,n}^{m',n'} &= \frac{e}{\hbar} \int_{m,n}^{m',n'} \mathbf{A}(\mathbf{r}) \cdot d\mathbf{r} \\ &= \frac{eB}{2\hbar} (x_m + x_{m'}) (y_{n'} - y_n),\end{aligned}\quad (3.26)$$

Here, the nineteen hopping coordinates considered up to TNN are given by  $x_m = \frac{ma}{2}$  ( $m = \pm 1, \pm 2$ ) and  $y_n = \frac{n a \sqrt{3}}{2}$  ( $n = 0, \pm 1$ ), where  $a$  is the lattice constant, are shown in Fig. 3.2. Details of the derivation of the Eq. (3.26) are given in Appendix B.

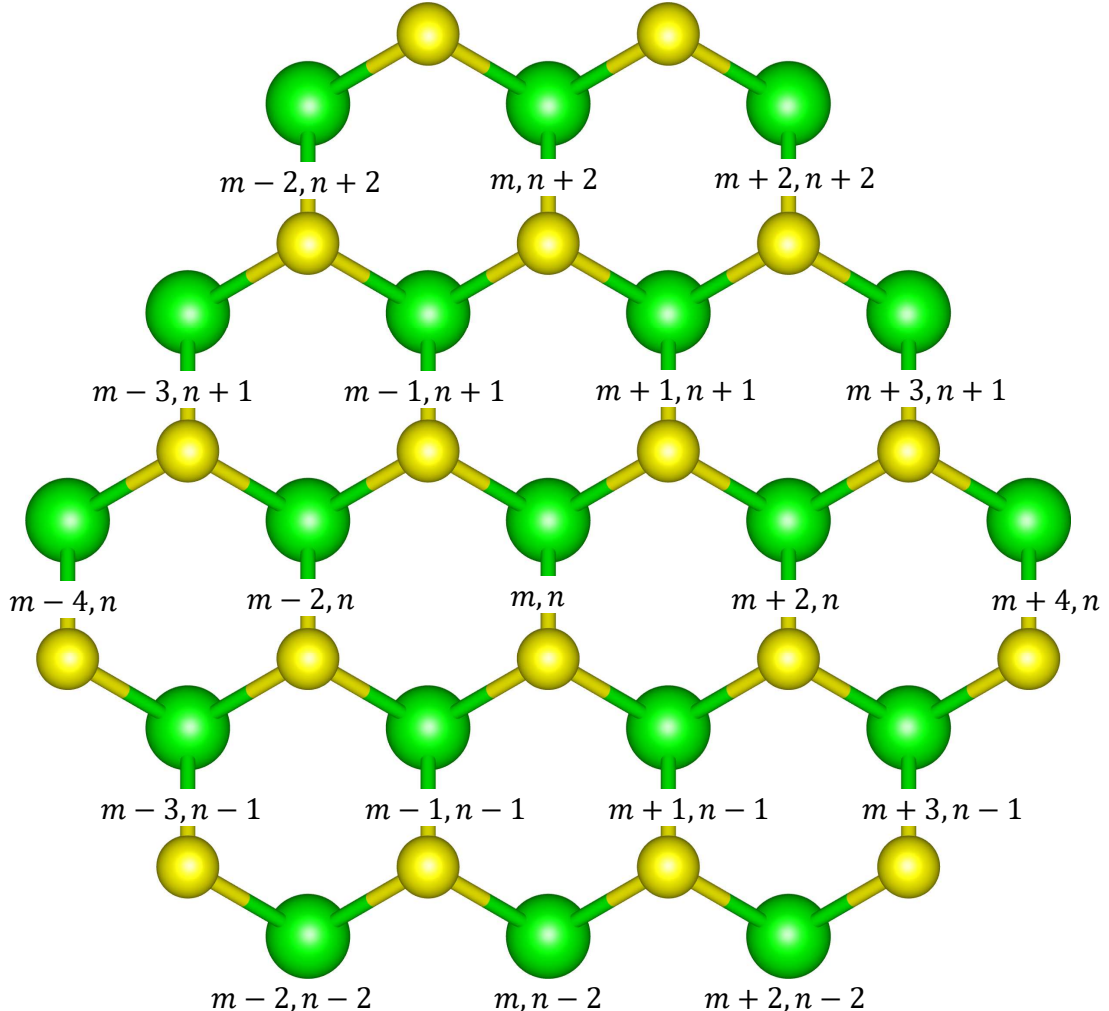


Figure 3.2: The TBM of TMD with eighteen neighbor atoms M rewrite with the site index.

Since  $dy = 0$  along the  $x$  direction,  $\theta_{m,n}^{m\pm 2,n} = 0$ , and using TNN coordinates given for

lattice site in Table 3.1, the  $\theta_{m,n}^{m',n'}$  can be written as

$$\theta_{m,n}^{m',n'} = \begin{cases} 0 & m' = m \pm 2, n' = n, \\ 0 & m' = m \pm 4, n' = n, \\ \pm \frac{e}{\hbar} \frac{Ba^2 \sqrt{3}}{2} m & m' = m, n' = n \pm 2, \\ \pm \frac{e}{\hbar} \frac{Ba^2 \sqrt{3}}{4} (m \mp \frac{1}{2}) & m' = m \mp 1, n' = n \pm 1, \\ \pm \frac{e}{\hbar} \frac{Ba^2 \sqrt{3}}{2} (m \mp 1) & m' = m \mp 2, n' = n \pm 2, \\ \pm \frac{e}{\hbar} \frac{Ba^2 \sqrt{3}}{4} (m \mp \frac{3}{2}) & m' = m \mp 3, n' = n \pm 1. \end{cases} \quad (3.27)$$

Identifying  $\frac{Ba^2 \sqrt{3}}{2}$  as the magnetic flux  $\Phi$  passing through per unit cell and  $\frac{\hbar}{e}$  corresponds to the magnetic flux quantum  $\Phi_0$ , we obtain the following relation

$$\begin{aligned} H_{jj'}(\mathbf{k}) = & \mathcal{E}_{jj'}(\mathbf{0}) + e^{i\mathbf{k}\cdot\mathbf{R}_1} \mathcal{E}_{jj'}(\mathbf{R}_1) + e^{-i\pi(m+1/2)\Phi/\Phi_0} e^{i\mathbf{k}\cdot\mathbf{R}_2} \mathcal{E}_{jj'}(\mathbf{R}_2) \\ & + e^{-i\pi(m-1/2)\Phi/\Phi_0} e^{i\mathbf{k}\cdot\mathbf{R}_3} \mathcal{E}_{jj'}(\mathbf{R}_3) + e^{i\mathbf{k}\cdot\mathbf{R}_4} \mathcal{E}_{jj'}(\mathbf{R}_4) \\ & + e^{i\pi(m-1/2)\Phi/\Phi_0} e^{i\mathbf{k}\cdot\mathbf{R}_5} \mathcal{E}_{jj'}(\mathbf{R}_5) + e^{i\pi(m+1/2)\Phi/\Phi_0} e^{i\mathbf{k}\cdot\mathbf{R}_6} \mathcal{E}_{jj'}(\mathbf{R}_6) \\ & + e^{-i\pi(m+3/2)\Phi/\Phi_0} e^{i\mathbf{k}\cdot\tilde{\mathbf{R}}_1} \mathcal{E}_{jj'}(\tilde{\mathbf{R}}_1) + e^{-2i\pi m \Phi / \Phi_0} e^{i\mathbf{k}\cdot\tilde{\mathbf{R}}_2} \mathcal{E}_{jj'}(\tilde{\mathbf{R}}_2) \\ & + e^{-i\pi(m-3/2)\Phi/\Phi_0} e^{i\mathbf{k}\cdot\tilde{\mathbf{R}}_3} \mathcal{E}_{jj'}(\tilde{\mathbf{R}}_3) + e^{i\pi(m-3/2)\Phi/\Phi_0} e^{i\mathbf{k}\cdot\tilde{\mathbf{R}}_4} \mathcal{E}_{jj'}(\tilde{\mathbf{R}}_4) \\ & + e^{2i\pi m \Phi / \Phi_0} e^{i\mathbf{k}\cdot\tilde{\mathbf{R}}_5} \mathcal{E}_{jj'}(\tilde{\mathbf{R}}_5) + e^{i\pi(m+3/2)\Phi/\Phi_0} e^{i\mathbf{k}\cdot\tilde{\mathbf{R}}_6} \mathcal{E}_{jj'}(\tilde{\mathbf{R}}_6) \\ & + e^{i\mathbf{k}\cdot\mathbf{R}'_1} \mathcal{E}_{jj'}(\mathbf{R}'_1) + e^{-2i\pi(m+1)\Phi/\Phi_0} e^{i\mathbf{k}\cdot\mathbf{R}'_2} \mathcal{E}_{jj'}(\mathbf{R}'_2) \\ & + e^{-2i\pi(m-1)\Phi/\Phi_0} e^{i\mathbf{k}\cdot\mathbf{R}'_3} \mathcal{E}_{jj'}(\mathbf{R}'_3) + e^{i\mathbf{k}\cdot\mathbf{R}'_4} \mathcal{E}_{jj'}(\mathbf{R}'_4) \\ & + e^{2i\pi(m-1)\Phi/\Phi_0} e^{i\mathbf{k}\cdot\mathbf{R}'_5} \mathcal{E}_{jj'}(\mathbf{R}'_5) + e^{2i\pi(m+1)\Phi/\Phi_0} e^{i\mathbf{k}\cdot\mathbf{R}'_6} \mathcal{E}_{jj'}(\mathbf{R}'_6). \end{aligned} \quad (3.28)$$

The Hamiltonian matrix element in Eq. (3.28) depends only on the site index  $m$  and does not invariant under the expansion of a lattice vector along the  $x$  axis. In order to restore this invariance, we can look at the case where the ratio of magnetic flux and flux quanta is a rational number  $\Phi/\Phi_0 = p/q$ . The crucial advantage of the Peierls phase approach is that it allows the lattice periodicity to be restored, provided that a suitable magnetic unit cell or “magnetic supercell” containing several original unit cells is constructed. One might ask what truly happens inside the magnetic unit cells. Do the neighbor interactions remain the same way as they did in the tight-binding model? We will explore this after deriving the Hamiltonian for the magnetic unit cell.

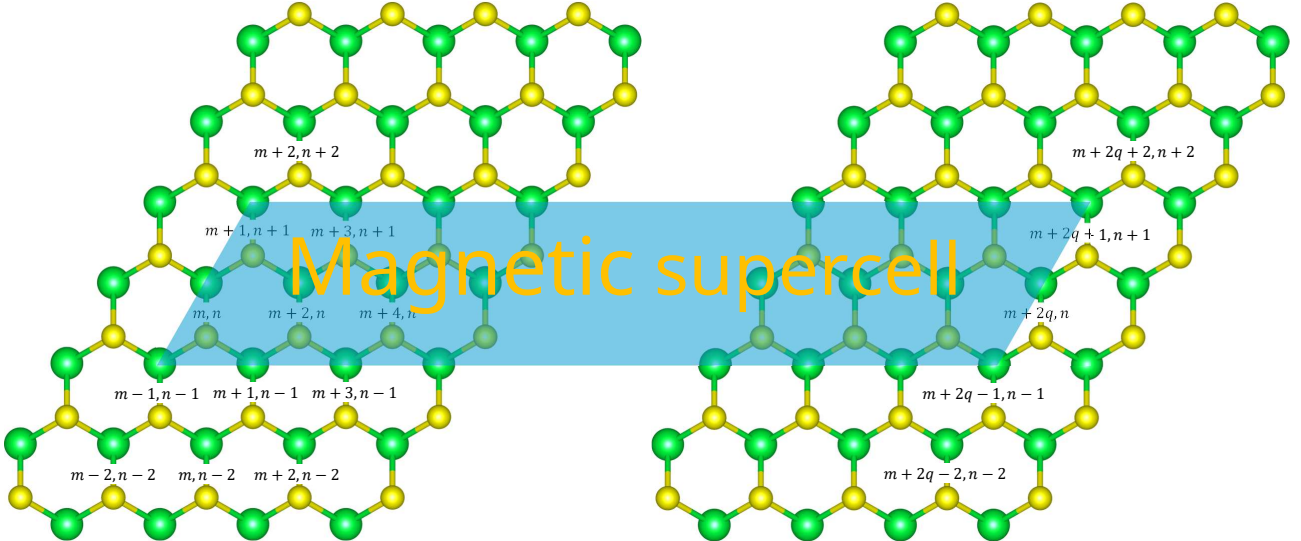


Figure 3.3: Magnetic unit cell for TMD monolayers.

In Section 3.1, we ignored the sum over of relative positions  $\mathbf{r}_i$  in Eq. (2.3) as the orbitals of X atoms were neglected. However, the magnetic unit cell consists  $2q$  atom M. We now define a new basis set of  $6q$  atomic orbitals  $\{\phi_j(\mathbf{r} - \mathbf{r}_i)\}$  where  $j = 1, 2, 3$  and  $\mathbf{r}_i \in \text{MUC}$ . The new basis function now is

$$\psi_{\lambda, \mathbf{k}}(\mathbf{r}) = \sum_j^3 \sum_i^{2q} C_{ji}^\lambda(\mathbf{k}) \sum_\alpha e^{i\mathbf{k}\cdot(\mathbf{R}_\alpha + \mathbf{r}_i)} \phi_j(\mathbf{r} - \mathbf{R}_\alpha - \mathbf{r}_i). \quad (3.29)$$

Here, we set  $\mathbf{r}_i$  refers to the position of an atom in a unit cell, while  $\mathbf{R}_\alpha$  denotes the position of different unit cells. The Hamiltonian matrix elements in the new basis is written as

$$\begin{aligned} H_{jj'}^{ii'}(\mathbf{k}) &= \sum_\alpha \sum_\beta e^{i\mathbf{k}\cdot(\mathbf{R}_\beta - \mathbf{R}_\alpha + \mathbf{r}_{i'} - \mathbf{r}_i)} \langle \phi_j(\mathbf{r} - \mathbf{R}_\alpha - \mathbf{r}_i) | \left[ -\frac{\hbar^2 \nabla^2}{2m} + U_0 \right] | \phi_j(\mathbf{r} - \mathbf{R}_\beta - \mathbf{r}_{i'}) \rangle \\ &= \sum_\alpha \sum_\beta e^{i\mathbf{k}\cdot(\mathbf{R}_\beta - \mathbf{R}_\alpha + \mathbf{r}_{m',n'} - \mathbf{r}_{m,n})} \langle \phi_j(\mathbf{r} - \mathbf{R}_\alpha - \mathbf{r}_{m,n}) | \left[ -\frac{\hbar^2 \nabla^2}{2m} + U_0 \right] | \phi_j(\mathbf{r} - \mathbf{R}_\beta - \mathbf{r}_{m',n'}) \rangle. \end{aligned} \quad (3.30)$$

Now we center our system at  $\mathbf{r}' = \mathbf{r} - \mathbf{R}_\alpha - \mathbf{r}_{m,n}$  and define  $\mathbf{R}_\gamma = \mathbf{R}_\alpha - \mathbf{R}_\beta$ . We get

$$H_{jj'}^{ii'}(\mathbf{k}) = \sum_\alpha \sum_\gamma e^{-i\mathbf{k}\cdot(\mathbf{R}_\gamma + \mathbf{r}_{m,n} - \mathbf{r}_{m',n'})} \langle \phi_j(\mathbf{r}) | \left[ -\frac{\hbar^2 \nabla^2}{2m} + U_0 \right] | \phi_j(\mathbf{r} + \mathbf{R}_\gamma + \mathbf{r}_{m,n} - \mathbf{r}_{m',n'}) \rangle. \quad (3.31)$$

Taking the sum over  $\mathbf{R}_\gamma$  considering only NN, NNN, TNN such that  $|\mathbf{R}_\gamma| \leq a$ . The lattice vectors that satisfying this condition is  $\mathbf{R}_\gamma = 0$ . Since only the NN, NNN and TNN are considered, the matrix elements  $\langle \phi_j(\mathbf{r}) | \left[ -\frac{\hbar^2 \nabla^2}{2m} + U_0 \right] | \phi_j(\mathbf{r} + \mathbf{r}_{m,n} - \mathbf{r}_{m',n'}) \rangle$  are nonzero when  $\mathbf{r}_{m',n'} = \mathbf{r}_{m,n} + \mathbf{R}$ , where  $\mathbf{R} = 0$  or a displacement vector connecting

to a NN, NNN, TNN atoms, the Hamiltonian matrix elements are written in the form

$$H_{jj'}^{ii'}(\mathbf{k}) = \sum_{\mathbf{R}} e^{i\mathbf{k}\cdot\mathbf{R}} \langle \phi_j(\mathbf{r}) | \left[ -\frac{\hbar^2 \nabla^2}{2m} + U_0(\mathbf{r}) \right] | \phi_{j'}(\mathbf{r} - \mathbf{R}) \rangle \delta_{m+\Delta m_{\mathbf{R}}, m'} \delta_{n+\Delta n_{\mathbf{R}}, n'}, \quad (3.32)$$

here  $(\Delta m_{\mathbf{R}}, \Delta n_{\mathbf{R}})$  the hopping relative coordinates are given in Table 3.1.

One can recognize that Eq. (3.32) resembles Eq. (3.4). Additionally, the equation not only describes the hopping between magnetic unit cells but also accounts for hopping between sites within magnetic unit cells. To address the previous question, it is important to note that we have enlarged the original unit cell into a magnetic unit cell, which now contains  $2q$  atoms M. The neighbor interactions are preserved inside the “supercell”, but they now involve neighboring magnetic unit cells due to the enlarged cell structure. The Hamiltonian has a discrete translational invariance with a unit cell carrying  $2q$  unit cells along the  $x$  axis.

The Hamiltonian with the Peierls phase now is

$$H_{jj'}^{ii'}(\mathbf{k}) = \sum_{\mathbf{R}} e^{i\theta_{m,n}^{m+\Delta m_{\mathbf{R}}, n+\Delta n_{\mathbf{R}}}} e^{i\mathbf{k}\cdot\mathbf{R}} \langle \phi_j(\mathbf{r}) | \left[ -\frac{\hbar^2 \nabla^2}{2m} + U_0(\mathbf{r}) \right] | \phi_{j'}(\mathbf{r} - \mathbf{R}) \rangle \delta_{m+\Delta m_{\mathbf{R}}, m'} \delta_{n+\Delta n_{\mathbf{R}}, n'}. \quad (3.33)$$

Simplifying Eq. (3.33), we get the Hamiltonian for the magnetic unit cell

$$\begin{aligned} H_{jmjn'm'n'}(\mathbf{k}) = & \mathcal{E}_{jj'}(\mathbf{0}) \delta_{m,m'} \delta_{n,n'} + e^{i\mathbf{k}\cdot\mathbf{R}_1} \mathcal{E}_{jj'}(\mathbf{R}_1) \delta_{m+2,m'} \delta_{n,n'} + e^{i\mathbf{k}\cdot\mathbf{R}_4} \mathcal{E}_{jj'}(\mathbf{R}_4) \delta_{m-2,m'} \delta_{n,n'} \\ & + e^{-i\pi(m+1/2)\Phi/\Phi_0} e^{i\mathbf{k}\cdot\mathbf{R}_2} \mathcal{E}_{jj'}(\mathbf{R}_2) \delta_{m+1,m'} \delta_{n-1,n'} + e^{-i\pi(m-1/2)\Phi/\Phi_0} e^{i\mathbf{k}\cdot\mathbf{R}_3} \mathcal{E}_{jj'}(\mathbf{R}_3) \delta_{m-1,m'} \delta_{n-1,n'} \\ & + e^{i\pi(m-1/2)\Phi/\Phi_0} e^{i\mathbf{k}\cdot\mathbf{R}_5} \mathcal{E}_{jj'}(\mathbf{R}_5) \delta_{m-1,m'} \delta_{n+1,n'} + e^{i\pi(m+1/2)\Phi/\Phi_0} e^{i\mathbf{k}\cdot\mathbf{R}_6} \mathcal{E}_{jj'}(\mathbf{R}_6) \delta_{m+1,m'} \delta_{n+1,n'} \\ & + e^{-i\pi(m+3/2)\Phi/\Phi_0} e^{i\mathbf{k}\cdot\tilde{\mathbf{R}}_1} \mathcal{E}_{jj'}(\tilde{\mathbf{R}}_1) \delta_{m+3,m'} \delta_{n-1,n'} + e^{-2i\pi m \Phi/\Phi_0} e^{i\mathbf{k}\cdot\tilde{\mathbf{R}}_2} \mathcal{E}_{jj'}(\tilde{\mathbf{R}}_2) \delta_{m,m'} \delta_{n-2,n'} \\ & + e^{-i\pi(m-3/2)\Phi/\Phi_0} e^{i\mathbf{k}\cdot\tilde{\mathbf{R}}_3} \mathcal{E}_{jj'}(\tilde{\mathbf{R}}_3) \delta_{m-3,m'} \delta_{n-1,n'} + e^{i\pi(m-3/2)\Phi/\Phi_0} e^{i\mathbf{k}\cdot\tilde{\mathbf{R}}_4} \mathcal{E}_{jj'}(\tilde{\mathbf{R}}_4) \delta_{m-3,m'} \delta_{n+1,n'} \\ & + e^{2i\pi m \Phi/\Phi_0} e^{i\mathbf{k}\cdot\tilde{\mathbf{R}}_5} \mathcal{E}_{jj'}(\tilde{\mathbf{R}}_5) \delta_{m,m'} \delta_{n+2,n'} + e^{i\pi(m+3/2)\Phi/\Phi_0} e^{i\mathbf{k}\cdot\tilde{\mathbf{R}}_6} \mathcal{E}_{jj'}(\tilde{\mathbf{R}}_6) \delta_{m+3,m'} \delta_{n+1,n'} \\ & + e^{i\mathbf{k}\cdot\mathbf{R}'_1} \mathcal{E}_{jj'}(\mathbf{R}'_1) \delta_{m+4,m'} \delta_{n,n'} + e^{-2i\pi(m+1)\Phi/\Phi_0} e^{i\mathbf{k}\cdot\mathbf{R}'_2} \mathcal{E}_{jj'}(\mathbf{R}'_2) \delta_{m+2,m'} \delta_{n-2,n'} \\ & + e^{-2i\pi(m-1)\Phi/\Phi_0} e^{i\mathbf{k}\cdot\mathbf{R}'_3} \mathcal{E}_{jj'}(\mathbf{R}'_3) \delta_{m-2,m'} \delta_{n-2,n'} + e^{i\mathbf{k}\cdot\mathbf{R}'_4} \mathcal{E}_{jj'}(\mathbf{R}'_4) \delta_{m-4,m'} \delta_{n,n'} \\ & + e^{2i\pi(m-1)\Phi/\Phi_0} e^{i\mathbf{k}\cdot\mathbf{R}'_5} \mathcal{E}_{jj'}(\mathbf{R}'_5) \delta_{m-2,m'} \delta_{n+2,n'} + e^{2i\pi(m+1)\Phi/\Phi_0} e^{i\mathbf{k}\cdot\mathbf{R}'_6} \mathcal{E}_{jj'}(\mathbf{R}'_6) \delta_{m+2,m'} \delta_{n+2,n'}. \end{aligned} \quad (3.34)$$

Now, for given flux ratio  $p/q$ , only the  $q$  determines the periodicity of the magnetic cell assuming  $p$  and  $q$  are mutually prime numbers. Eq. (3.34) give the following matrix

which must be diagonalized to obtain the energy eigenvalues

$$H^{\text{TB}} = \begin{pmatrix} V_0 & V_1 & V_2 \\ V_1^* & V_{11} & V_{12} \\ V_2^* & V_{12}^* & V_{22} \end{pmatrix}, \quad (3.35)$$

with

$$H_{jj'}^{\text{TB}} = \begin{pmatrix} A_{jj'}^{(0)} & B_{jj'}^{(0)} & C_{jj}^{(0)} & D_{jj'}^{(0)} & E_{jj'}^{(0)} & F_{jj'}^{(0)} & 0 & \cdots & G_{jj'}^{(0)} & H_{jj'}^{(0)} & I_{jj'}^{(0)} & K_{jj'}^{(0)} \\ K_{jj'}^{(1)} & A_{jj'}^{(1)} & B_{jj'}^{(1)} & C_{jj'}^{(1)} & D_{jj'}^{(1)} & E_{jj'}^{(1)} & F_{jj'}^{(1)} & 0 & \cdots & G_{jj'}^{(1)} & H_{jj'}^{(1)} & I_{jj'}^{(1)} \\ I_{jj'}^{(2)} & K_{jj'}^{(2)} & A_{jj'}^{(2)} & B_{jj'}^{(2)} & C_{jj'}^{(2)} & D_{jj'}^{(2)} & E_{jj'}^{(2)} & F_{jj'}^{(2)} & 0 & \cdots & G_{jj'}^{(2)} & H_{jj'}^{(2)} \\ \vdots & \vdots \\ C_{jj'}^{(q-2)} & \dots & \dots & \dots & \dots & \dots & \dots & 0 & \cdots & K_{jj'}^{(q-2)} & A_{jj'}^{(q-2)} & B_{jj'}^{(q-2)} \\ B_{jj'}^{(q-1)} & C_{jj'}^{(q-1)} & \dots & \dots & \dots & \dots & \dots & \dots & 0 & \cdots & K_{jj'}^{(q-1)} & A_{jj'}^{(q-1)} \end{pmatrix}, \quad (3.36)$$

where  $A_{jj'}^{(m)}$  is the hopping with the relative coordinates  $(m, n)$ ,  $B_{jj'}^{(m)}$  is the hopping with the relative coordinates  $(m+1, n)$ , and so on, and  $V_0, V_1, V_2, V_{11}, V_{12}, V_{22}$  are submatrices of size  $6q \times 6q$ , see Fig. 3.4.

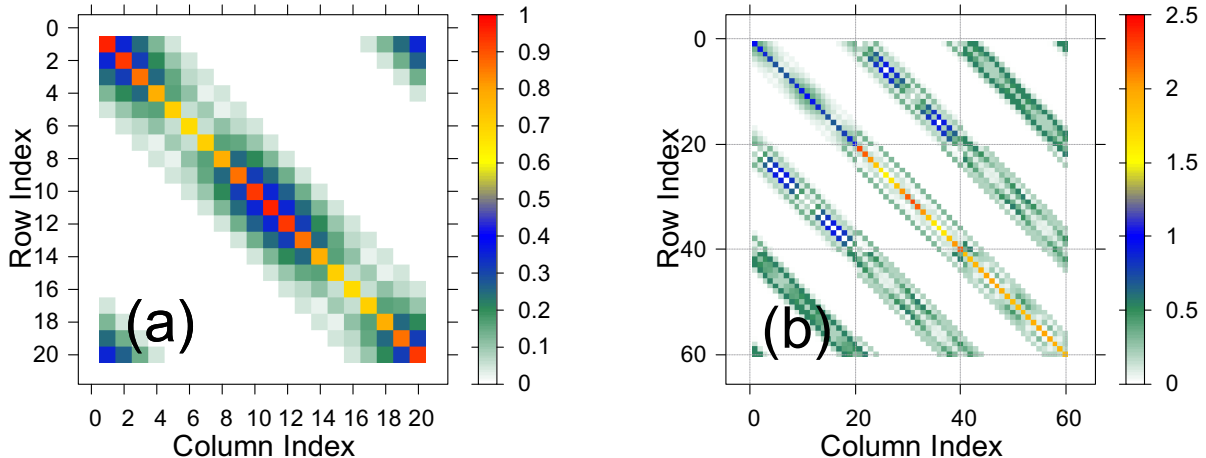


Figure 3.4: An simple and intuitive visualization of sub-matrix  $V_0$  for single-band(a) and matrix  $H$  for three band(b) using standard plotter with  $q = 10$ .

## CHAPTER 4

### RESULTS AND DISCUSSION

To illustrate the applicability of the three-band TBM developed in Chapter 3, we consider the case of monolayer MoS<sub>2</sub> as a representative example of TMDs. For completeness, similar calculations have been performed for other TMD monolayers. The corresponding results are provided in Appendix B.

#### 4.1 Band structure of MoS<sub>2</sub> at zero magnetic field

We begin the analysis by calculating the band structure of monolayer MoS<sub>2</sub> using the three-band tight-binding model that includes spin-orbit coupling (SOC). This model captures the essential features of the low-energy physics near the  $K$  and  $K'$  points of the Brillouin zone.

By solving the Hamiltonian in Eq. (3.11), we obtain the eigenvalues of the Hamiltonian, which are evaluated across the entire Brillouin zone. These are computed over all  $k$ -points throughout the entire Brillouin zone (BZ), and the corresponding band structure is illustrated in Fig. 4.1. The presence of three orbitals from the M atom in the unit cell results in three energy bands: one valence band (VB) and two conduction bands (CBs). When spin-orbit coupling is included, these bands split due to spin degeneracy, leading to six bands in total. Among them, the VB exhibits a prominent spin splitting near the  $K$  and  $K'$  points, while the CBs remain nearly degenerate.

This splitting is attributed to the atomic SOC of the Mo atom, with a magnitude of  $\Delta_{\text{SOC}}^{\lambda} = 2\lambda = 146$  meV. This effect is a hallmark of monolayer TMDs, playing a crucial role in spin-valley coupling and valley-selective optical properties.

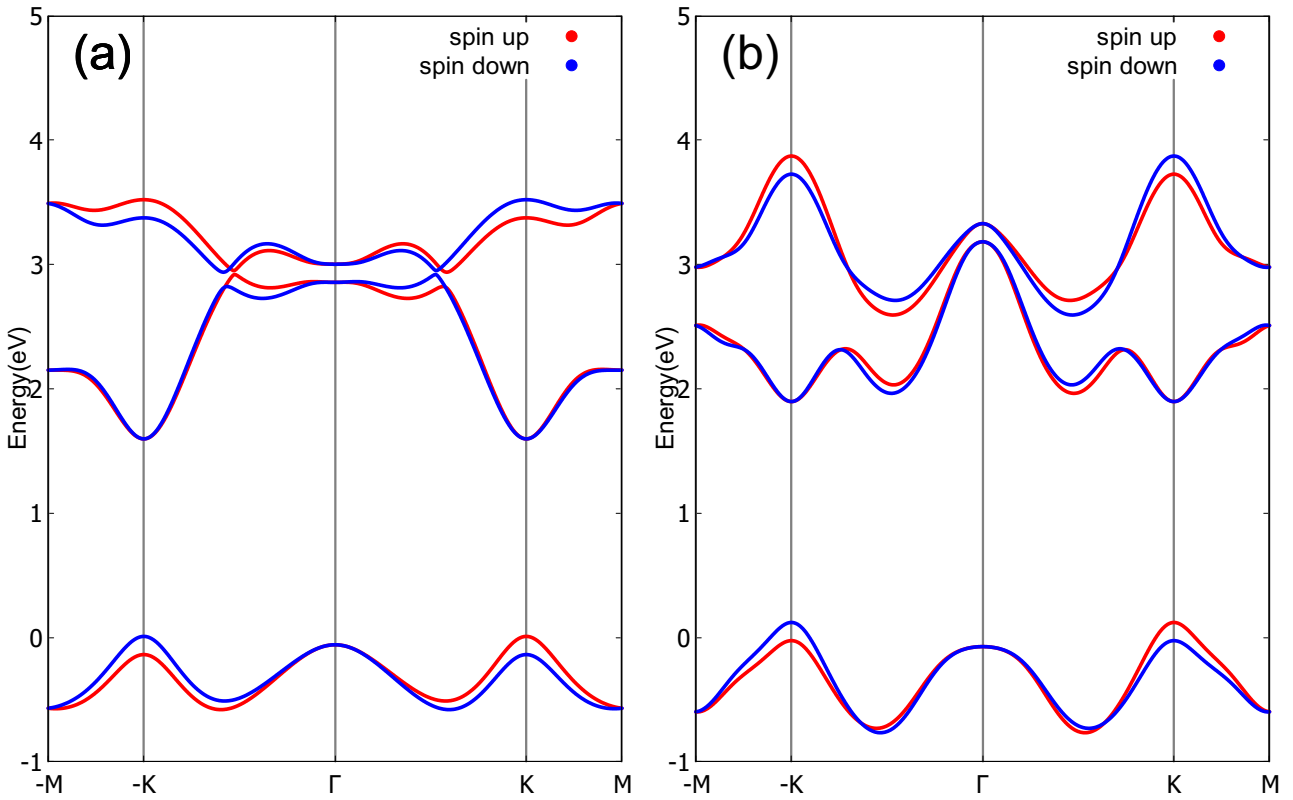


Figure 4.1: The band structure of monolayer MoS<sub>2</sub> in the absence of a magnetic field along the  $\Gamma$ -K direction exhibits significant spin splittings at the  $K$  and  $-K$  points, primarily due to spin-orbit coupling (SOC). Figures 4.1(a) and 4.1(b) show the results obtained using NN and TNN model, respectively.

## 4.2 Hofstadter butterfly of monolayer MoS<sub>2</sub>

In this section, we explore the Hofstadter spectrum by presents the solution of Eq. 3.35. By plotting the band energies while varying the  $p$ , we obtain the famous Hofstadter butterfly [9], a complex fractal structure as seen in Fig. 4.2. This fractal spectrum is a result of two competing effects, lattice periodicity and magnetic unit cell periodicity enforced by the presence of the magnetic field. The magnetic field enters the TB Hamiltonian only through the fraction  $p/q$ , which is proportional to the magnetic flux through the primitive unit cell of the lattice. In general, as the lattice geometry evolves, the area of the primitive unit cell changes  $m$  times.

In this study, the Hofstadter butterfly of MoS<sub>2</sub> is generated at the  $K$ -point. Additionally, we compute a single-band Hofstadter butterfly (using only the conduction band) to highlight the underlying triangular lattice structure of MoS<sub>2</sub>. In Fig. 4.2, for the NN model, the Hofstadter butterfly structure clearly resembles that of a triangular lattice, as previously reported in other materials such as [10].

Another observation is that the lattice constant  $a$  and the magnetic field  $B$  always appears together in an expression with the magnetic field ( $\frac{Ba^2\sqrt{3}}{2}$ ). This quantity reflects

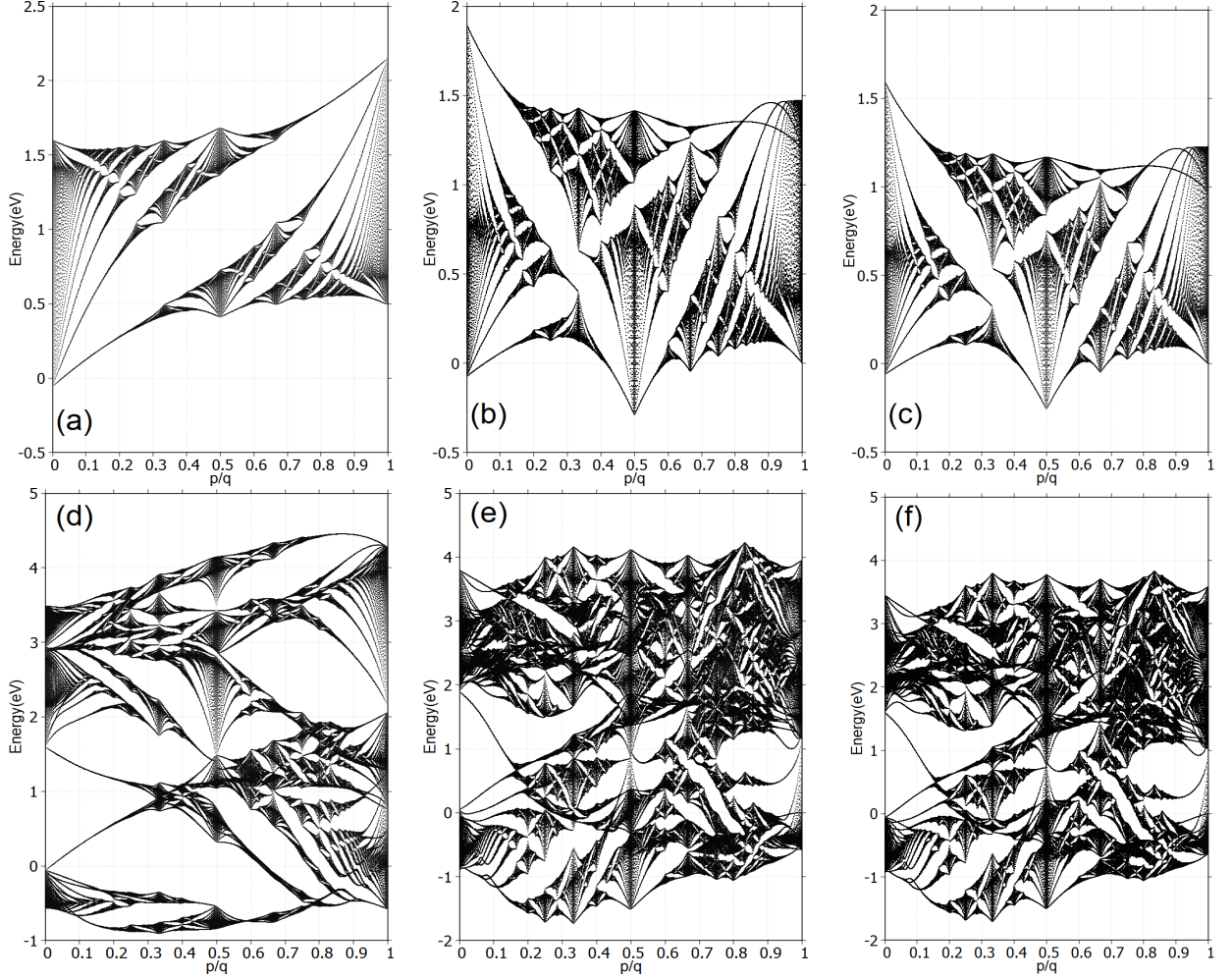


Figure 4.2: Hofstadter butterfly for single-band  $|dz\rangle \equiv |\phi_1^1(x, y)\rangle$  (a,b,c) and all band (d,e,f) for NN and TNN for MoS<sub>2</sub>, respectively, with  $q = 797$  and vary  $p$  from 1 to  $q$  with field strength  $B_0 = 4.6928 \times 10^4$  T. Here on  $x$ -axis represents the flux in units of quantum flux enclosed by the unit cell and  $y$ -axis represents the Energy. While (b,e) use generalized-gradient approximation (GGA) parameter, (c,f) use local-density approximation (LDA) one.

the flux per plaquette in the super magnetic unit cell, which is relevant in the context of Aharonov-Bohm effect [11]. Since the expression involves the product  $Ba^2$ , this implies that increasing  $B$  by a certain amount is mathematically equivalent to increasing  $a$ . In other words, for energy calculations, increasing the strength of the magnetic field is physically equivalent to increasing the lattice constant, as both affect the system in the same way through the flux per unit cell. In addition, the three-band spectrum contains a complex and rich physics insight but it seems remains the fractal structure. The main energy bands are basically LLs, which we shall discuss in the next Section. For small values of the magnetic flux ratio  $p/q$ , these LLs manifest sharp and well-separated energy bands. However, when increasing  $p$  from 1 to  $q$ , each LLs go a recursive splitting into  $2q$  subbands. This structure arises from the magnetic unit cell's periodicity.

The spectrum exhibits several noticeable symmetries. First, it depends only on

the flux ratio  $p/q$ , meaning that shifting  $p/q$  by an integer  $c$  (i.e.,  $p/q \rightarrow p/q + c$ ) leaves the spectrum unchanged. Additionally, the spectrum remains invariant under the transformation  $p/q \rightarrow -p/q$ , since if  $\psi$  is an eigenstate with energy  $E$  for flux  $p/q$ , its complex conjugate  $\psi^*$  is an eigenstate with the same energy for flux  $-p/q$ . These two symmetries are general and not specific to the MoS<sub>2</sub> case. However, the third symmetry involves changing  $p/q$  to  $p/q+1/2$ , which is equivalent to flipping the sign of the hopping energies  $t_i$  (i.e.,  $t_i \rightarrow -t_i$ ), resulting in an inversion of the spectrum, which is concealed clearly in square lattice [9] or honeycomb lattice [12]. In contrast, for the case MoS<sub>2</sub>, the flux going through a unit cell is already one half, making this symmetry hidden. In fact, by adding an integer  $n$  to the Peierls phase, one can effectively recover this symmetry, but this modification does not correspond to any physical observable.

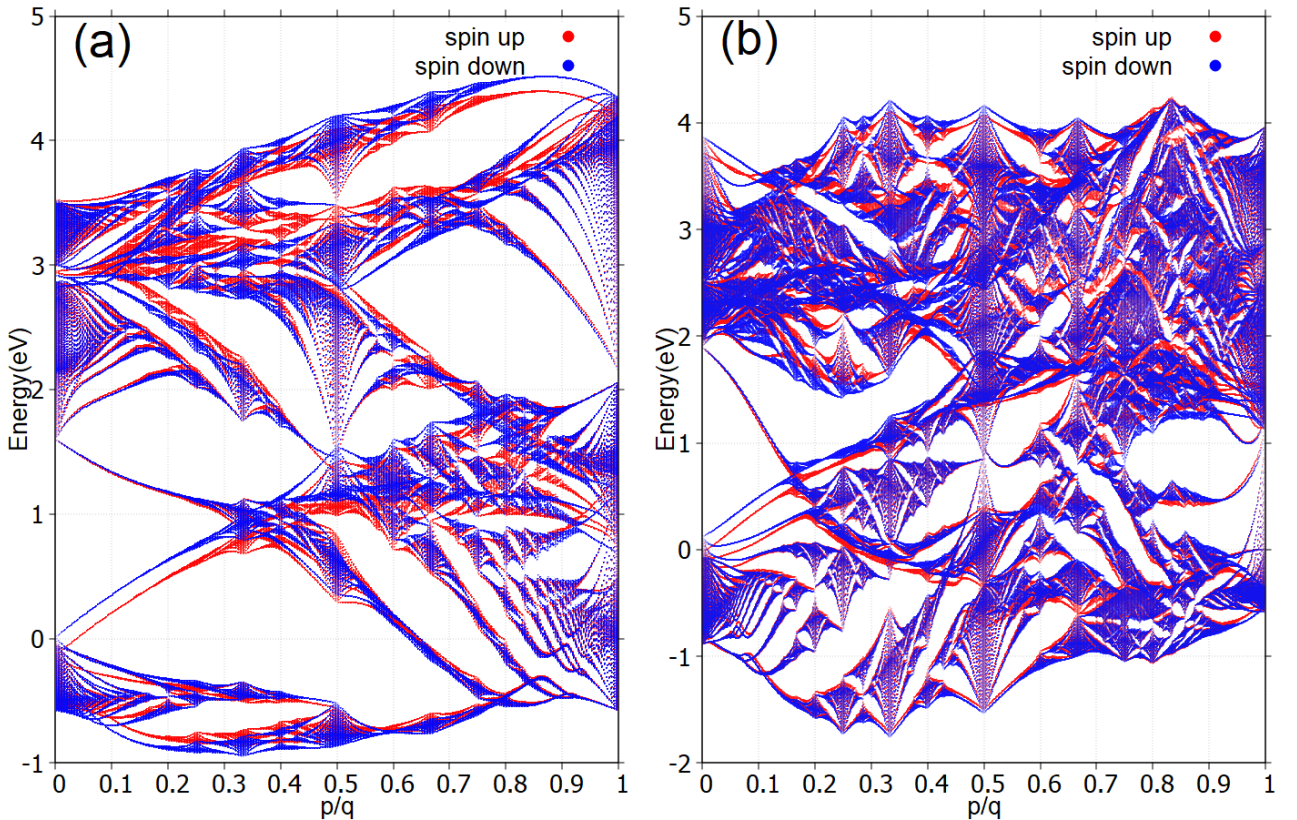


Figure 4.3: Hofstadter butterfly of monolayer MoS<sub>2</sub> with SOC at  $K$  point. Figures 4.3(a) and 4.3(b) show the results obtained using NN and TNN model, respectively.

The role of the eight hopping constants  $t$  is just to set an energy scale. Change the hopping constants amounts to stretching the butterfly spectrum vertically, which is an overall scaling to the energy levels. Thus it does not give rise to any interesting physical phenomenon.

At the very large magnetic fields, the magnetic strength overwhelms the effects of SOC. In this work, we treat the SOC interaction as an adjustable constant in the Hamiltonian. As a result, the SOC induces a spin splitting in the Hofstadter spectrum,

see in Fig. 4.3.

In the case of the NN model for MoS<sub>2</sub>, our results are consistent with those reported in Refs. [2, 3]. However, it is worth noting that our approach is more general, as Eq. (3.34) explicitly incorporates the variation of  $\delta_{n,n'}$ , which was not considered in their formulation, such as in the equations of Refs. [3] or Eq. 5 of Refs. [2]. In addition, we also take into account interactions with 18 neighboring atoms, a level of detail that, to the best of our knowledge, has not been included in earlier models. This extended consideration significantly increases the computational complexity and demands.

### 4.3 Landau levels in monolayer MoS<sub>2</sub>

The approach in Section 2.3 is for free electrons, but near the bottom of the two-dimensional tight-binding band of TMD we must find a regime in which the electron behaves as a nearly one(At least with a nearly free dispersion relation).

Recalling the result obtained for the dispersion relation of an electron within the TBM

$$H_{11} = 2t_0(\cos 2\alpha + 2 \cos \alpha \cos \beta) + \epsilon_1. \quad (4.1)$$

The dispersion energy is approximately free-electron-like by Taylor expansion to second order of  $\mathbf{k}$

$$\begin{aligned} H_{11}(\mathbf{k}) &\approx 2t_0 \left[ 1 - \frac{a^2 k_x^2}{2} + 2 \left( 1 - \frac{a^2 k_x^2}{8} \right) \left( 1 - \frac{3a^2 k_y^2}{8} \right) \right] \\ &= t_0 \frac{3}{16} \left( 32 + a^4 k_x^2 k_y^2 \right) - t_0 \frac{3}{2} a^2 \left( k_x^2 + k_y^2 \right) + \epsilon_1, \end{aligned} \quad (4.2)$$

the term  $a^4$  is negligibly small, then we have

$$H_{11}(\mathbf{k}) \approx 6t_0 - \frac{3}{2} t_0 a^2 (k_x^2 + k_y^2) + \epsilon_1. \quad (4.3)$$

One of the ways derivation of effective mass  $m^*$  is substitution  $\hbar\mathbf{k} \rightarrow \mathbf{\Pi} + e\mathbf{A}$ , with Landau gauge  $\mathbf{A} = (0, Bx, 0)$

$$\begin{aligned} H_{11}(\mathbf{\Pi}) &\approx 6t_0 - \frac{3}{2} t_0 \frac{a^2}{\hbar^2} \left[ \Pi_x^2 + (\Pi_y + eBx)^2 \right] + \epsilon_1 \\ &\approx 6t_0 - \frac{3}{2} t_0 \frac{a^2}{\hbar^2} \Pi_x^2 - \frac{3}{2} t_0 \frac{a^2}{\hbar^2} (eB)^2 \left[ x - \left( -\frac{\hbar k_y}{eB} \right) \right]^2 + \epsilon_1. \end{aligned} \quad (4.4)$$

The Eq (4.4) can be rewrite in the form as

$$E(\mathbf{\Pi}) = 6t_0 - \left[ \frac{1}{2m^*} \Pi_x^2 + \frac{1}{2} m^* \omega_c^2 (x - x_0)^2 \right] + \epsilon_1, \quad (4.5)$$

where  $m^* = \frac{\hbar^2}{3t_0 a^2}$  is the effective mass and  $x_0 = \frac{\hbar k_y}{eB}$ . Subsequently, the cyclotron frequency is

$$\omega_c = \frac{eB}{m^*} = \frac{8\pi\sqrt{3}t_0}{\hbar} \frac{p}{q}, \quad (4.6)$$

and therefore the Landau levels near the bottom of the band structure can be written as

$$\begin{aligned} E_n &= 6t_0 - \hbar\omega_c(n + 1/2) + \epsilon_1 \\ &= t_0 \left( 6 - 8\pi\sqrt{3} \frac{p}{q} (n + 1/2) \right) + \epsilon_1, \end{aligned} \quad (4.7)$$

in linear order of an uniform-flux, where  $n$  is Landau index.

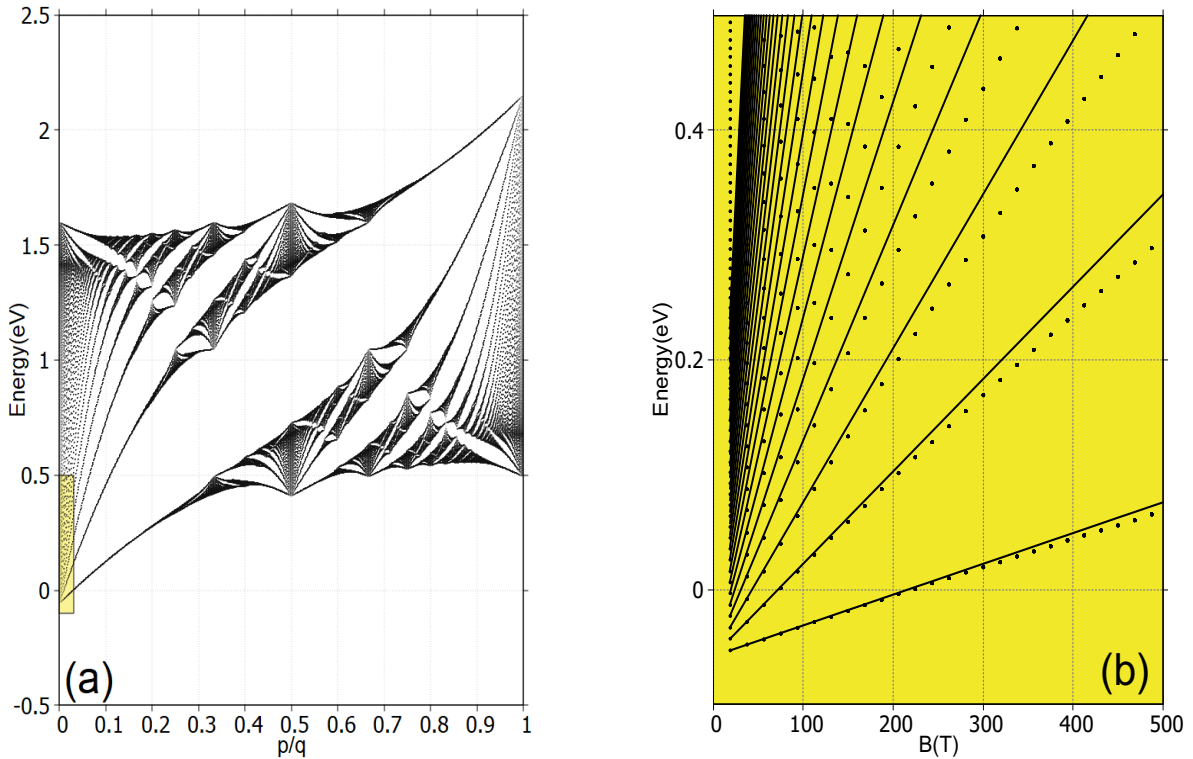


Figure 4.4: (a) Same plot as Fig. 4.4(a) but considering a small area and (b) shows both the Landau fan diagram and the Hofstadter butterfly. Display the first  $n = 30$  levels near the bottom of the conduction band for a magnetic field up to  $B = 500$  T.

In Fig. 4.4 we compare the spectrum of a small section of single-band with  $p/q = 1/797$ , which is equivalent to small magnetic field, the spectrum of MoS<sub>2</sub>, with the energy of Landau levels given by Eq. (4.7) show standard equally spaced LLs [13–16] near the bottom of the bands, as plotted in Fig. 4.4(b). The fan of LLs can be clearly

seen emerging from the pattern in Fig. 4.4(a).

In Fig. 4.4(a), there is just single-band in case zero field, with the effective mass  $m^* = \frac{\hbar}{3t_0a^2}$ . The numerical result for this portion of the spectrum are shown in Fig. 4.4 for  $p/q \geq 1/797$ . The first few LLs are clearly seen, and the asymptotic slopes  $p/q$  at large  $q$  given by Eq. (4.7) are shown for comparison for the first five Landau levels at  $B \leq 100$  T. At the values of  $B$  the fit is not ideal, but it does seem to be improving with the decreasing  $p/q$ .

Figure 4.4 also displays a blowup of the low uniform magnetic field region, showing the LLs as a function of  $\Phi/\Phi_0$ . These Landau levels appear approximately linear in  $B$ , which is a consequence of magnetic quantization of the parabolic bands at  $B = 0$  T. As the magnetic field increases, the LLs are sequentially depopulated. For example, at  $B = 200$  T, the levels are completely filled up to  $n = 4$ , whereas at  $B = 500$  T, only levels up to  $n = 1$  remain filled, and higher levels are emptied. When compared with the theoretical study presented in Section 2.3, we find that the Hofstadter butterfly in the weak magnetic field regime is in excellent agreement with the predicted Landau level structure. This indicates that the model accurately captures the low-field physics.

## 4.4 Color the Hofstadter butterfly

In Section 2.4.2, we arrived at the Hall conductivity equation from a single subband, which is given by [17–20]

$$\sigma_{xy} = \frac{e^2}{h} \sum_n^{\text{occ.}} \frac{1}{2\pi} \iint_{\text{BZ}} dk_x dk_y \Omega_n^z(\mathbf{k}). \quad (4.8)$$

In general, the Berry curvature integrated over a closed manifold is quantized in the units of  $e^2/h$  and equals to the net number of monopoles inside. This number is called the Chern number and is responsible for a number of quantization effects. Therefore the Hall conductivity is quantized for a two dimensional band insulator of noninteracting electrons. By integrating the Berry curvature over the entire Brillouin zone, we arrived at the Thouless-Kohmoto-Nightingale-Nijs (TKNN)’s formula [20]

$$\sigma_{xy} = \frac{e^2}{h} \nu, \quad \nu = 1, 2, \dots \quad (4.9)$$

$\nu$  is the Chern number.

We, then, calculate the quantum Hall conductivity by the Streda formula [21]

$$\sigma_{xy}(B, E_F) = e \frac{\partial N(E, B)}{\partial B} \Big|_{E=E_F}, \quad (4.10)$$

where  $N(E_F, B)$  is the number of state at fixed Fermi energy  $E_F$ . Combining Eq. (4.9) and Eq. (4.10), we have

$$\frac{\partial N}{\partial B} = \frac{e}{h} \nu. \quad (4.11)$$

Assuming that  $B$  vary slightly

$$N = c + \frac{e}{h} B \nu, \quad c \text{ is constant.} \quad (4.12)$$

Before this, we have defined  $\frac{p}{q} = \frac{eBa^2\sqrt{3}}{2h}$ , with  $S = \frac{\sqrt{3}a^2}{2}$  is the area of the original unit cell in Section 3.2. Multiply  $S$  with Eq. (4.12), we have

$$N \times S = c + \frac{p}{q} \nu, \quad (4.13)$$

and the density of electron in a single band is given by  $\frac{1}{Sq}$ , thus when there are  $r$  bands below the Fermi energy level, the density of electron for  $r^{\text{th}}$  band is

$$N = \frac{r}{Sq}. \quad (4.14)$$

Then, the Eq. (4.13), is written as,

$$r = c \times q + p \times \nu_r, \quad (4.15)$$

in this equation  $r, q, p, \nu$  are integers, thus,  $c \times q$  must be an integer. On the one hand, since  $c$  is independent of  $q$ , then  $c$  itself must be an integer, namely  $s_r$ . Thus we have

$$r = q \times s_r + p \times \nu_r, \quad (4.16)$$

this equation is usually named as the Diophantine equation. While  $\nu_r$  is the Chern number associated with the quantized Hall conductance which can be found by taking  $\nu_r$  between  $-q/2$  and  $q/2$  and determining its allows conductance to be determined,  $s$  is another integer that play a role in indentify the gap index.

The Hall conductivity of the lattice model for an electron in a background magnetic field can only be computed when the flux ratio  $\frac{\Phi}{\Phi_0} = \frac{p}{q}$  is rational. In this case, we

can use the TKNN formula, but with the Chern number, which used to be defined by intergrating over the Brillouin zone, now arising by intergrating over the magnetic Brillouin zone. Others derivation is in [22–24].

The Diophantine equation is crucial in understanding the quantization of Hall conductance in the Hofstadter butterfly. The Chern number  $\nu$  determines the topological nature of the bands and their contribution to the Hall conductance, while the integer  $s$  identifies specific energy gaps in the spectrum. These gaps are directly linked to incompressible quantum Hall states, which are of significant interest in both theoretical and experimental condensed matter physics. The solutions to the Diophantine equation are presented in Table D.1 in Appendix D, revealing many interesting observations can be extracted from it. Firstly, we observe the occurence values of  $\nu = \pm 1$  at both  $r = p$  and  $r = q - p$ . This owing to each band being devided into  $q$  subbands. Significantly, the case  $r = p$ , where the corresponding gap index naturally corresponds to the first gap in the Landau level. The second observation is the symmetry of the table, the value of  $\nu_r$  is equal to  $-\nu_{q-r}$ . This is due, once again, to the symmetry of the butterfly.

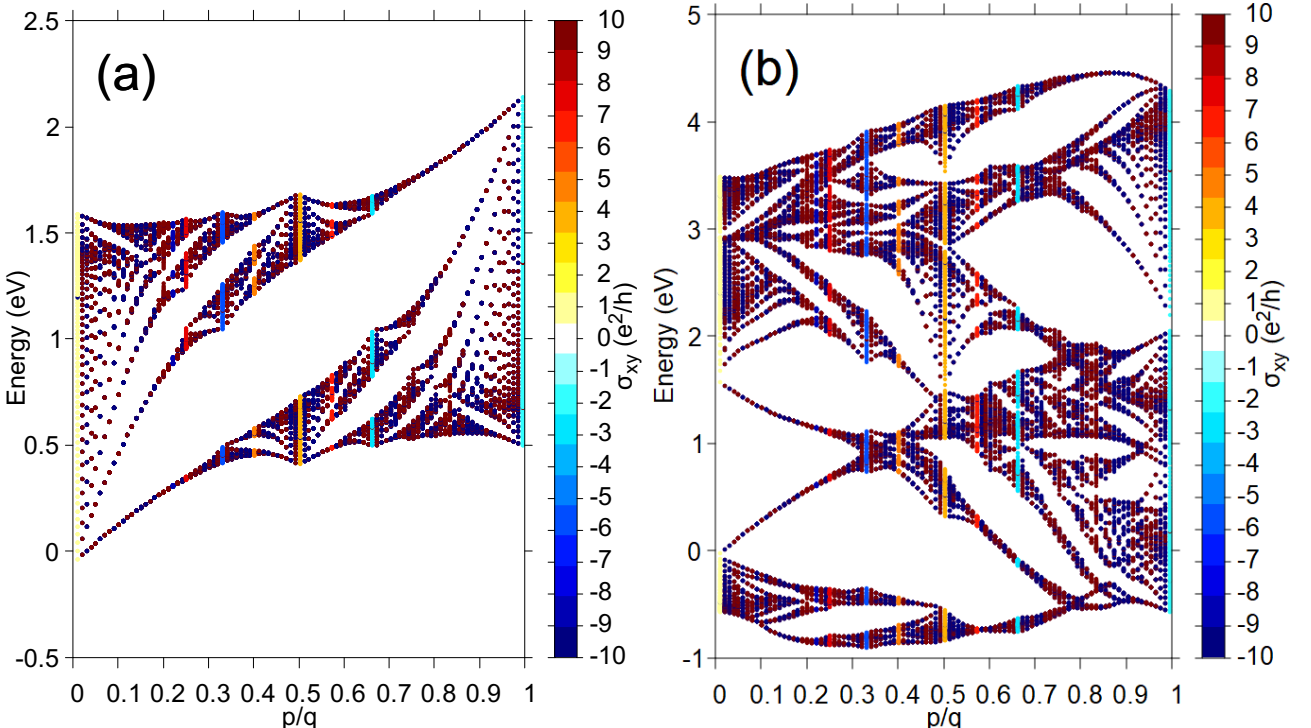


Figure 4.5: Colored points version of Hofstadter butterfly.

To further explore the intricate fractal nature of the Hofstadter spectrum, we shall now achieve the colored Hofstadter butterfly. There are many ways to color the butterfly. For instance, a common approach is to color each point of the butterfly based on their Chern number, as illustrated in the Fig. 4.5. At these points, the Hall conductivity hightlights exactly quantization. However, a drawback of this method is that the butterfly may contain a dense of points, which can make it difficult to visualise fine

details in the colored spectrum.

Figures 4.6 and 4.7 displays the Hofstadter butterfly, color-coded according to the Hall conductance. Moreover, the number  $p$  increases simultaneously with Chern number, making it challenging to maintain a fixed scale. Addressing this, we limit the Chern number scale within  $-10 \leq \nu \leq 10$ , any Chern number outside this range is set to zero. Regions with zero Hall conductance and the corresponding spectrum are left blank. Remarkably, the two largest gaps near the center of the figure are associated with small integers where the color coding accurately reflects their values. This idea was first made by Avron *et al*[24].

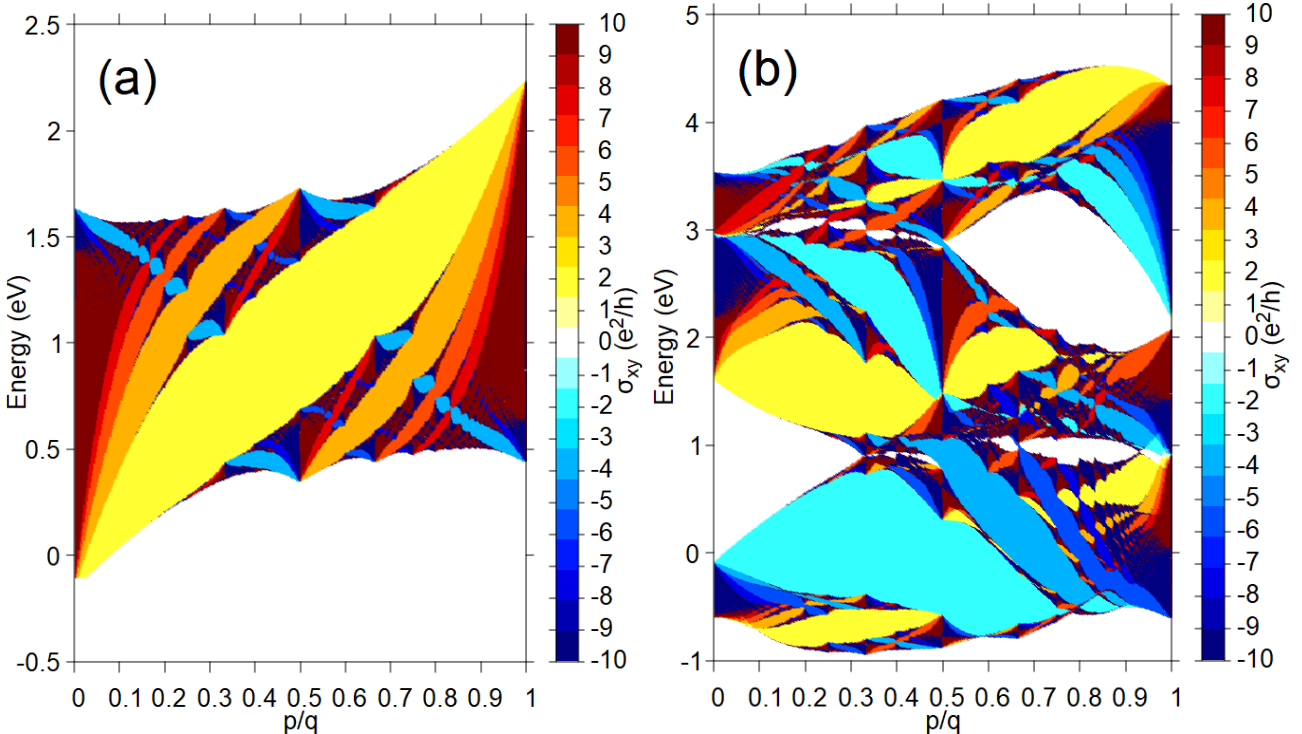


Figure 4.6: Gaps color-coded Hofstadter butterfly. Figures 4.6(a) and 4.6(b) show the results obtained using only NN for single band and three band, respectively.

Both figures display rich physics insights, it totally use two different methods to color the butterfly. While Fig. 4.5 assigns colors based on the sum of the Chern numbers of the occupied bands, Figs. 4.6 and 4.7 color the gap according to the Chern number that corresponded to each gap index. However, the colored spectrum do more than highlighting the topological properties of the system, they both also explain the behaviour of electrons in a symmetry lattice. Unlike the traditional Hofstadter butterfly, which highlights the energy spectrum, this version emphasizes the energy gaps by applying a color scheme to indicate different Hall conductance values. Each color represents a distinct quantized Hall conductance. Such as, doping a fixed number of electrons will cause Fermi level change, which is reflected in changes to the Density of state (DOS), captured in Fig. 4.6. In addition as the magnetic field increases, there are fewer bands

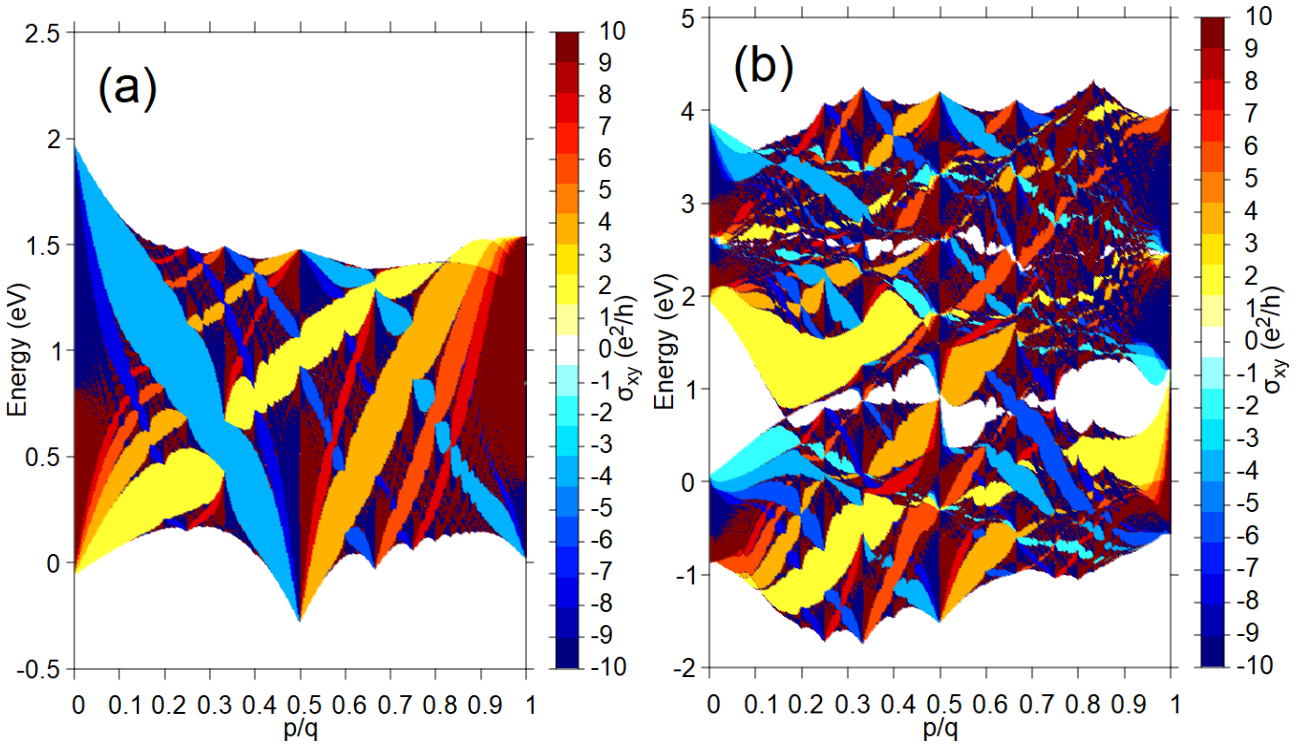


Figure 4.7: Gaps color-coded Hofstadter butterfly for TNN case. Figures 4.7(a) and 4.7(b) show the results for single band and three band, respectively.

occupied. One might ask where the electrons goes. They still there, but not in the bands.

## 4.5 Conclusions

In our research, we have investigated the Hofstadter butterfly spectrum of monolayer MoS<sub>2</sub> and other transition metal dichalcogenides (TMDs) using a tight-binding three-band model. In the presence of an external magnetic field, we have explored various quantum phenomena such as Landau levels and the integer quantum Hall effect (IQHE). The results demonstrate the intricate interplay between the periodic lattice and the magnetic field, leading to rich topological structures in the electronic spectrum.

In Section 4.1, we introduced the three-band tight-binding model for monolayer MX<sub>2</sub>, focusing only on the metal  $d_{z^2}$ ,  $d_{xy}$ , and  $d_{x^2-y^2}$  orbitals. By incorporating up to third-nearest-neighbor (TNN) hoppings, and utilizing the  $D_{3h}$  point group symmetry, we derived nineteen hopping parameters as originally presented in Ref. [1].

Section 4.2 examined the Hofstadter physics in monolayer TMDs. We demonstrated that when subjected to a perpendicular magnetic field, the system develops a fractal energy spectrum, strongly influenced by spin-orbit coupling (SOC) and giving rise to topological quantum Hall states.

Sections 4.3 and 4.4 extended the theoretical analysis to include Landau quantization and Hall conductivity. In particular, we showed how the Hofstadter butterfly can be enriched and visualized through Chern number calculations.

Importantly, our results successfully reproduce previous findings reported in the literature, confirming the accuracy of our implementation. More significantly, this thesis presents several novel contributions: it incorporates third-nearest-neighbor (TNN) hoppings, which were previously neglected in earlier works, and integrates the quantum Hall effect directly into the Hofstadter butterfly spectrum. To the best of our knowledge, this unified framework—combining topological characterization with a full tight-binding calculation of the Hofstadter spectrum—has not been previously explored in such a comprehensive and systematic manner.

Despite these insights, several limitations remain. For instance, in Section 4.4, our calculations of the Chern number were restricted to the single-band approximation due to the numerical complexity of the full three-band system. Computing Chern numbers in a multi-band framework is computationally demanding, especially for larger Hamiltonians. In our experience, generating a high-resolution color-mapped Hofstadter butterfly based on Chern numbers took approximately two days of computation.

In conclusion, we have demonstrated how the Hofstadter butterfly and IQHE emerge in monolayer TMDs using a three-band tight-binding approach. Group theory was employed to constrain the hopping parameters. The NN model by Liu *et al.* accurately reproduces the highest valence band near the  $K$  point but fails to match the conduction bands and other regions of the Brillouin zone. In contrast, the TNN model, which includes nineteen parameters, yields a much better overall description of all three bands (two conduction bands and one valence band) indicating that both NN and TNN M–M hoppings play a crucial role.

However, since these models include only the  $d$  orbitals of metal atoms, they are limited in describing systems with defects or contributions from chalcogen atoms. Furthermore, while the NN model may suffice for basic applications, more sophisticated systems require the extended TNN model to capture the full physical picture.

Overall, the Hofstadter butterfly serves as a powerful tool to probe both the topological and quantum Hall physics in 2D materials. Future studies that build upon this work, particularly those exploring more complex or novel 2D materials, will continue to deepen our understanding of condensed matter phenomena.

## APPENDIX A

### Derivation of anomalous Hall conductivity

We begin with the electric current density in Eq. (2.31)

$$\begin{aligned}
J_x &= \frac{e}{\hbar L^2} \sum_{n,\mathbf{k}} \frac{\partial \varepsilon_n(\mathbf{k})}{\partial k_x} f_n(\mathbf{k}) + \frac{e^2}{\hbar L^2} E_y \sum_{n,\mathbf{k}} \Omega_\nu^z(\mathbf{k}) f_n(\mathbf{k}) \\
&\approx \frac{e}{\hbar 4\pi^2} \left[ \sum_{\nu}^{\text{occ.}} \iint_{\text{BZ}} dk_x dk_y \frac{\partial \varepsilon_\nu(\mathbf{k})}{\partial k_x} + 2 \iint d^2\mathbf{k} \frac{\partial \varepsilon_{\nu'}(\mathbf{k})}{\partial k_x} f_{\nu'}(\mathbf{k} + \Delta\mathbf{k}) \right] \\
&\quad + \frac{e^2}{\hbar 4\pi^2} E_y \left[ \sum_{\nu}^{\text{occ.}} \iint dk_x dk_y \Omega_\nu + 2 \iint d^2\mathbf{k} \Omega_{\nu'}^z(\mathbf{k}) f_{\nu'}(\mathbf{k} + \Delta\mathbf{k}) \right], \tag{A.1}
\end{aligned}$$

in which  $\Delta\mathbf{k} = -e\mathbf{E}\tau/\hbar$ . Using the dispersion relation  $\varepsilon_{\nu'}(\mathbf{k}) \simeq \frac{\hbar\mathbf{k}^2}{2m}$ , the second term now is

$$\begin{aligned}
\iint d^2\mathbf{k} \frac{\partial \varepsilon_{\nu'}(\mathbf{k})}{\partial k_x} f_{\nu'}(\mathbf{k} + \Delta\mathbf{k}) &= \iint d^2\mathbf{k} \frac{\partial \varepsilon_{\nu'}(\mathbf{k} - \Delta\mathbf{k})}{\partial k_x} f_{\nu'}(\mathbf{k}) \\
&= \int_0^{2\pi} d\phi \int_0^{k_F} k dk \frac{\hbar^2}{2m} \left( k \cos \phi + \frac{eE_x\tau}{\hbar} \right) = \frac{\pi k_F^2 \hbar e E_x \tau}{m}, \tag{A.2}
\end{aligned}$$

where  $k_F = \sqrt{2\pi\nu}$ . Substituting Eq. (A.3) into Eq. (A.2), the electric current density now is

$$\begin{aligned}
j_x &\approx \frac{ne^2\tau}{m} E_x + \frac{e^2}{\hbar 4\pi^2} E_y \left[ \sum_n^{\text{occ.}} \iint_{\text{BZ}} dk_x dk_y \Omega_\nu^z(\mathbf{k}) + 2 \iint d^2\mathbf{k} \Omega_{\nu'}^z(\mathbf{k}) f_{\nu'}(\mathbf{k} + \Delta\mathbf{k}) \right] \\
&\equiv \sigma_{xx} E_x + \sigma_{xy} E_y. \tag{A.3}
\end{aligned}$$

Therefore, the Hall conductivity now is

$$\sigma_{xy} = \frac{e^2}{h} \sum_n^{\text{occ.}} \frac{1}{2\pi} \iint_{\text{BZ}} dk_x dk_y \Omega_n^z(\mathbf{k}). \tag{A.4}$$

## APPENDIX B

### Matrix elements of the TB Hamiltonian without SOC

In this appendix, we show the matrix elements of the TB Hamiltonian in the absence of SOC. In addition, we provide the tight-binding parameters and Hofstadter spectra for other TMD monolayers as supplementary material.

$$\begin{aligned} \mathcal{E}(\mathbf{R}_2) &= D(\sigma'_\nu)\mathcal{E}(\mathbf{R}_1)D^\dagger(\sigma'_\nu) \\ &= \begin{pmatrix} t_0 & \frac{1}{2}t_1 - \frac{\sqrt{3}}{2}t_2 & -\frac{\sqrt{3}}{2}t_1 - \frac{1}{2}t_2 \\ -\frac{1}{2}t_1 - \frac{\sqrt{3}}{2}t_2 & \frac{1}{4}t_{11} + \frac{3}{4}t_{22} & -\frac{\sqrt{3}}{4}t_{11} - t_{12} + \frac{\sqrt{3}}{4}t_{22} \\ \frac{\sqrt{3}}{2}t_1 - \frac{1}{2}t_2 & -\frac{\sqrt{3}}{4}t_{11} + t_{12} + \frac{\sqrt{3}}{4}t_{22} & \frac{3}{4}t_{11} + \frac{1}{4}t_{22} \end{pmatrix}, \end{aligned} \quad (\text{B.1})$$

$$\begin{aligned} \mathcal{E}(\mathbf{R}_3) &= D(C(-\frac{2\pi}{3}))\mathcal{E}(\mathbf{R}_1)D^\dagger(C(-\frac{2\pi}{3})) \\ &= \begin{pmatrix} t_0 & -\frac{1}{2}t_1 + \frac{\sqrt{3}}{2}t_2 & -\frac{\sqrt{3}}{2}t_1 - \frac{1}{2}t_2 \\ \frac{1}{2}t_1 + \frac{\sqrt{3}}{2}t_2 & \frac{1}{4}t_{11} + \frac{3}{4}t_{22} & \frac{\sqrt{3}}{4}t_{11} + t_{12} - \frac{\sqrt{3}}{4}t_{22} \\ \frac{\sqrt{3}}{2}t_1 - \frac{1}{2}t_2 & \frac{\sqrt{3}}{4}t_{11} - t_{12} - \frac{\sqrt{3}}{4}t_{22} & \frac{3}{4}t_{11} + \frac{1}{4}t_{22} \end{pmatrix}, \end{aligned}$$

$$\mathcal{E}(\mathbf{R}_4) = D(\sigma_\nu)\mathcal{E}(\mathbf{R}_1)D^\dagger(\sigma_\nu) = \begin{pmatrix} t_0 & -t_1 & t_2 \\ t_1 & t_{11} & -t_{12} \\ t_2 & t_{12} & t_{22} \end{pmatrix}, \quad (\text{B.2})$$

$$\begin{aligned} \mathcal{E}(\mathbf{R}_5) &= D(C(-\frac{4\pi}{3}))\mathcal{E}(\mathbf{R}_1)D^\dagger(C(-\frac{4\pi}{3})) \\ &= \begin{pmatrix} t_0 & -\frac{1}{2}t_1 - \frac{\sqrt{3}}{2}t_2 & \frac{\sqrt{3}}{2}t_1 - \frac{1}{2}t_2 \\ \frac{1}{2}t_1 - \frac{\sqrt{3}}{2}t_2 & \frac{1}{4}t_{11} + \frac{3}{4}t_{22} & -\frac{\sqrt{3}}{4}t_{11} + t_{12} + \frac{\sqrt{3}}{4}t_{22} \\ -\frac{\sqrt{3}}{2}t_1 - \frac{1}{2}t_2 & -\frac{\sqrt{3}}{4}t_{11} - t_{12} + \frac{\sqrt{3}}{4}t_{22} & \frac{3}{4}t_{11} + \frac{1}{4}t_{22} \end{pmatrix}, \end{aligned} \quad (\text{B.3})$$

$$\begin{aligned} \mathcal{E}(\mathbf{R}_6) &= D(\sigma''_\nu)\mathcal{E}(\mathbf{R}_1)D^\dagger(\sigma''_\nu) \\ &= \begin{pmatrix} t_0 & \frac{1}{2}t_1 + \frac{\sqrt{3}}{2}t_2 & \frac{\sqrt{3}}{2}t_1 - \frac{1}{2}t_2 \\ -\frac{1}{2}t_1 + \frac{\sqrt{3}}{2}t_2 & \frac{1}{4}t_{11} + \frac{3}{4}t_{22} & \frac{\sqrt{3}}{4}t_{11} - t_{12} - \frac{\sqrt{3}}{4}t_{22} \\ -\frac{\sqrt{3}}{2}t_1 - \frac{1}{2}t_2 & \frac{\sqrt{3}}{4}t_{11} - t_{12} - \frac{\sqrt{3}}{4}t_{22} & \frac{3}{4}t_{11} + \frac{1}{4}t_{22} \end{pmatrix}, \end{aligned}$$

$$\begin{aligned}
\mathcal{E}(\tilde{\mathbf{R}}_2) &= D(C(-\frac{4\pi}{3}))\mathcal{E}(\tilde{\mathbf{R}}_4)D^\dagger(C(-\frac{4\pi}{3})) \\
&= \begin{pmatrix} r_0 & 0 & \frac{2r_2}{\sqrt{3}} \\ 0 & r_{11} + \sqrt{3}r_{12} & 0 \\ \frac{2r_1}{\sqrt{3}} & 0 & r_{11} - \frac{r_{12}}{\sqrt{3}} \end{pmatrix}, \\
\mathcal{E}(\tilde{\mathbf{R}}_3) &= D(\sigma_\nu)\mathcal{E}(\tilde{\mathbf{R}}_1)D^\dagger(\sigma_\nu) \\
&= \begin{pmatrix} r_0 & -r_1 & -\frac{r_1}{\sqrt{3}} \\ -r_2 & r_{11} & -r_{12} \\ -\frac{r_2}{\sqrt{3}} & -r_{12} & r_{11} + \frac{2r_{12}}{\sqrt{3}} \end{pmatrix}, \\
\mathcal{E}(\tilde{\mathbf{R}}_5) &= D(C(-\frac{4\pi}{3}))\mathcal{E}(\tilde{\mathbf{R}}_1)D^\dagger(C(-\frac{4\pi}{3})) \\
&= \begin{pmatrix} r_0 & 0 & \frac{2r_1}{\sqrt{3}} \\ 0 & r_{11} + \sqrt{3}r_{12} & 0 \\ \frac{2r_2}{\sqrt{3}} & 0 & r_{11} - \frac{r_{12}}{\sqrt{3}} \end{pmatrix}, \\
\mathcal{E}(\tilde{\mathbf{R}}_6) &= D(\sigma_\nu)\mathcal{E}(\tilde{\mathbf{R}}_4)D^\dagger(\sigma_\nu) \\
&= \begin{pmatrix} r_0 & -r_2 & -\frac{r_2}{\sqrt{3}} \\ -r_1 & r_{11} & -r_{12} \\ -\frac{r_1}{\sqrt{3}} & -r_{12} & r_{11} + \frac{2r_{12}}{\sqrt{3}} \end{pmatrix},
\end{aligned} \tag{B.4}$$

$$\begin{aligned}
\mathcal{E}(\mathbf{R}'_2) &= D(\sigma'_\nu)\mathcal{E}(\mathbf{R}'_1)D^\dagger(\sigma'_\nu) \\
&= \begin{pmatrix} u_0 & \frac{1}{2}u_1 - \frac{\sqrt{3}}{2}u_2 & -\frac{\sqrt{3}}{2}u_1 - \frac{1}{2}u_2 \\ -\frac{1}{2}u_1 - \frac{\sqrt{3}}{2}u_2 & \frac{1}{4}u_{11} + \frac{3}{4}u_{22} & -\frac{\sqrt{3}}{4}u_{11} - u_{12} + \frac{\sqrt{3}}{4}u_{22} \\ \frac{\sqrt{3}}{2}u_1 - \frac{1}{2}u_2 & -\frac{\sqrt{3}}{4}u_{11} + u_{12} + \frac{\sqrt{3}}{4}u_{22} & \frac{3}{4}u_{11} + \frac{1}{4}u_{22} \end{pmatrix}, \\
\mathcal{E}(\mathbf{R}'_3) &= D(C(-\frac{2\pi}{3}))\mathcal{E}(\mathbf{R}'_1)D^\dagger(C(-\frac{2\pi}{3})) \\
&= \begin{pmatrix} u_0 & -\frac{1}{2}u_1 + \frac{\sqrt{3}}{2}u_2 & -\frac{\sqrt{3}}{2}u_1 - \frac{1}{2}u_2 \\ \frac{1}{2}u_1 + \frac{\sqrt{3}}{2}u_2 & \frac{1}{4}u_{11} + \frac{3}{4}u_{22} & \frac{\sqrt{3}}{4}u_{11} + u_{12} - \frac{\sqrt{3}}{4}u_{22} \\ \frac{\sqrt{3}}{2}u_1 - \frac{1}{2}u_2 & \frac{\sqrt{3}}{4}u_{11} - u_{12} - \frac{\sqrt{3}}{4}u_{22} & \frac{3}{4}u_{11} + \frac{1}{4}u_{22} \end{pmatrix},
\end{aligned} \tag{B.5}$$

$$\mathcal{E}(\mathbf{R}'_4) = D(\sigma_\nu)\mathcal{E}(\mathbf{R}'_1)D^\dagger(\sigma_\nu) = \begin{pmatrix} u_0 & -u_1 & u_2 \\ u_1 & u_{11} & -u_{12} \\ u_2 & u_{12} & u_{22} \end{pmatrix}, \tag{B.6}$$

$$\begin{aligned}
\mathcal{E}(\mathbf{R}'_5) &= D(C(-\frac{4\pi}{3}))\mathcal{E}(\mathbf{R}'_1)D^\dagger(C(-\frac{4\pi}{3})) \\
&= \begin{pmatrix} u_0 & -\frac{1}{2}u_1 - \frac{\sqrt{3}}{2}u_2 & \frac{\sqrt{3}}{2}u_1 - \frac{1}{2}u_2 \\ \frac{1}{2}u_1 - \frac{\sqrt{3}}{2}u_2 & \frac{1}{4}u_{11} + \frac{3}{4}u_{22} & -\frac{\sqrt{3}}{4}u_{11} + u_{12} + \frac{\sqrt{3}}{4}u_{22} \\ -\frac{\sqrt{3}}{2}u_1 - \frac{1}{2}u_2 & -\frac{\sqrt{3}}{4}u_{11} - u_{12} + \frac{\sqrt{3}}{4}u_{22} & \frac{3}{4}u_{11} + \frac{1}{4}u_{22} \end{pmatrix}, \\
\mathcal{E}(\mathbf{R}'_6) &= D(\sigma''_\nu)\mathcal{E}(\mathbf{R}'_1)D^\dagger(\sigma''_\nu) \\
&= \begin{pmatrix} u_0 & \frac{1}{2}u_1 + \frac{\sqrt{3}}{2}u_2 & \frac{\sqrt{3}}{2}u_1 - \frac{1}{2}u_2 \\ -\frac{1}{2}u_1 + \frac{\sqrt{3}}{2}u_2 & \frac{1}{4}u_{11} + \frac{3}{4}u_{22} & \frac{\sqrt{3}}{4}u_{11} - u_{12} - \frac{\sqrt{3}}{4}u_{22} \\ -\frac{\sqrt{3}}{2}u_1 - \frac{1}{2}u_2 & \frac{\sqrt{3}}{4}u_{11} - u_{12} - \frac{\sqrt{3}}{4}u_{22} & \frac{3}{4}u_{11} + \frac{1}{4}u_{22} \end{pmatrix}.
\end{aligned} \tag{B.7}$$

In Eqs. (B.1) to (B.14),  $t, u$  and  $r$  are the hopping parameters and  $D(g_n)$  is the matrix of the irreducible representation (see Tables B.1 and B.2).

	$a(\text{\AA})$	$\epsilon_1$	$\epsilon_2$	$t_0$	$t_1$	$t_2$	$t_{11}$	$t_{12}$	$t_{22}$
GGA									
MoS <sub>2</sub>	3.190	1.046	2.104	-0.184	0.401	0.507	0.218	0.338	0.057
WS <sub>2</sub>	3.191	1.130	2.275	-0.206	0.567	0.536	0.286	0.384	-0.061
MoSe <sub>2</sub>	3.326	0.919	2.065	-0.188	0.317	0.456	0.211	0.290	0.130
WSe <sub>2</sub>	3.325	0.943	2.179	-0.207	0.457	0.486	0.263	0.329	0.034
MoTe <sub>2</sub>	3.557	0.605	1.972	-0.169	0.228	0.390	0.207	0.239	0.252
WTe <sub>2</sub>	3.560	0.606	2.102	-0.175	0.342	0.410	0.233	0.270	0.190
LDA									
MoS <sub>2</sub>	3.129	1.238	2.366	-0.218	0.444	0.533	0.250	0.360	0.047
WS <sub>2</sub>	3.132	1.355	2.569	-0.238	0.626	0.557	0.324	0.405	-0.076
MoSe <sub>2</sub>	3.254	1.001	2.239	-0.222	0.350	0.488	0.244	0.314	0.129
WSe <sub>2</sub>	3.253	1.124	2.447	-0.242	0.506	0.514	0.305	0.353	0.025
MoTe <sub>2</sub>	3.472	0.618	2.126	-0.202	0.254	0.423	0.241	0.263	0.269
WTe <sub>2</sub>	3.476	0.623	2.251	-0.209	0.388	0.442	0.272	0.295	0.200

Table B.1: Fitted parameters in three-band NN TBM for both GGA and LDA cases for MX<sub>2</sub> [1].

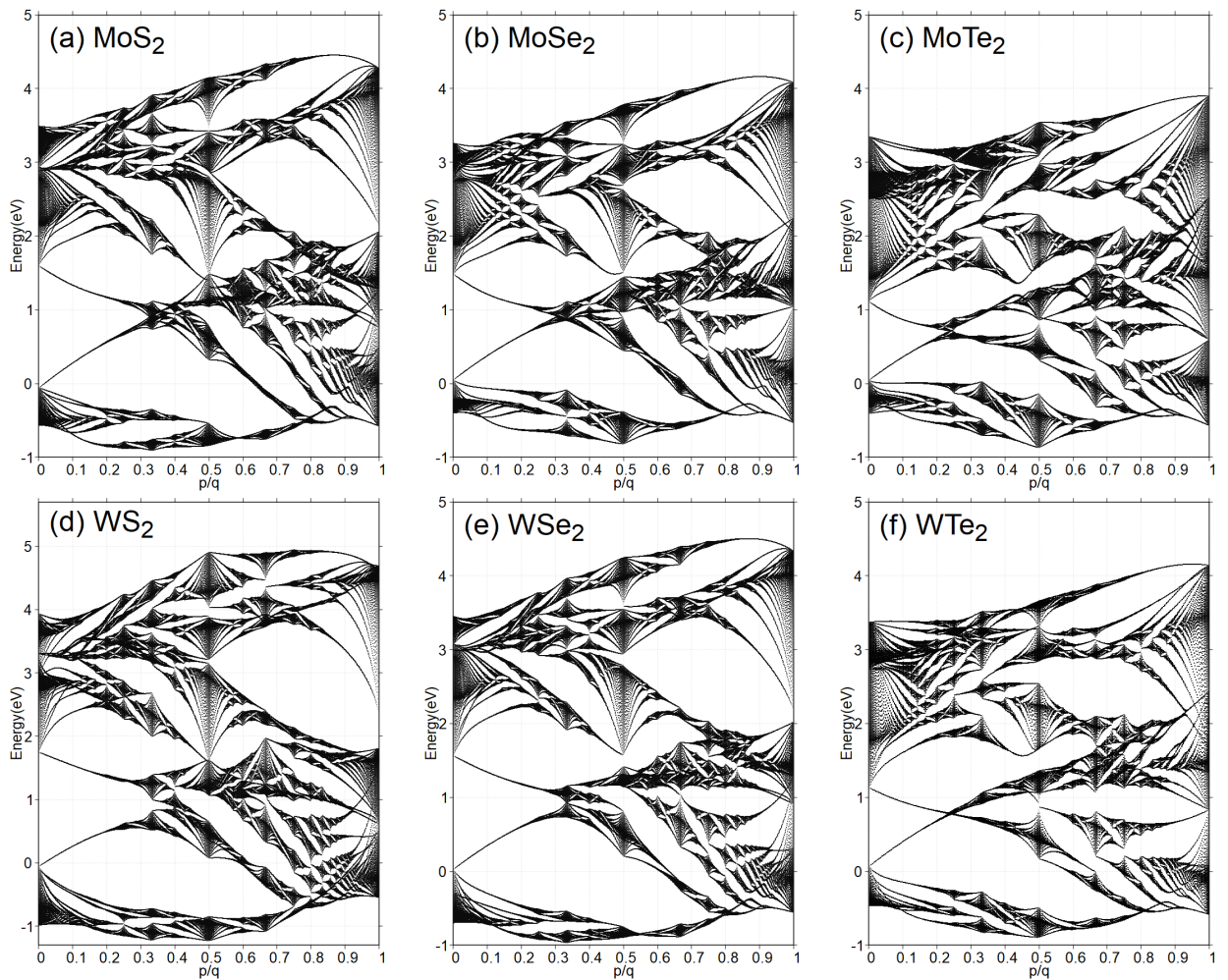


Figure B.1: The NN Hofstadter's butterflies of  $\text{MX}_2$  monolayers using GGA parameters from Table B.1.

	$a(\text{\AA})$	$\epsilon_1$	$\epsilon_2$	$t_0$	$t_1$	$t_2$	$t_{11}$	$t_{12}$	$t_{22}$	$r_0$
	$r_1$	$r_2$	$r_{11}$	$r_{12}$	$u_0$	$u_1$	$u_2$	$u_{11}$	$u_{12}$	$u_{22}$
GGA										
MoS <sub>2</sub>	3.190	0.683	1.707	-0.146	-0.114	0.506	0.085	0.162	0.073	0.060
	-0.236	0.067	0.016	0.087	-0.038	0.046	0.001	0.266	-0.176	-0.150
WS <sub>2</sub>	3.191	0.717	1.916	-0.152	-0.097	0.590	0.047	0.178	0.016	0.069
	-0.261	0.107	-0.003	0.109	-0.054	0.045	0.002	0.325	-0.206	-0.163
MoSe <sub>2</sub>	3.326	0.684	1.546	-0.146	-0.130	0.432	0.144	0.117	0.075	0.039
	-0.209	0.069	0.052	0.060	-0.042	0.036	0.008	0.272	-0.172	-0.150
WSe <sub>2</sub>	3.325	0.728	1.655	-0.146	-0.124	0.507	0.117	0.127	0.015	0.036
	-0.234	0.107	0.044	0.075	-0.061	0.032	0.007	0.329	-0.202	-0.164
MoTe <sub>2</sub>	3.357	0.588	1.303	-0.226	-0.234	0.036	0.400	0.098	0.017	0.003
	-0.025	-0.169	0.082	0.051	0.057	0.103	0.187	-0.045	-0.141	0.087
WTe <sub>2</sub>	3.560	0.697	1.380	-0.109	-0.164	0.368	0.204	0.093	0.038	-0.015
	-0.209	0.107	0.115	0.009	-0.066	0.011	-0.013	0.312	-0.177	-0.132
LDA										
MoS <sub>2</sub>	3.190	0.820	1.931	-0.176	-0.101	0.531	0.084	0.169	0.070	0.070
	-0.252	0.084	0.019	0.093	-0.043	0.047	0.005	0.304	-0.192	-0.162
WS <sub>2</sub>	3.191	0.905	2.167	-0.175	-0.090	0.611	0.043	0.181	0.008	0.075
	-0.282	0.127	0.001	0.114	-0.063	0.047	0.004	0.374	-0.224	-0.177
MoSe <sub>2</sub>	3.326	0.715	1.687	-0.154	-0.134	0.437	0.124	0.119	0.072	0.048
	-0.248	0.090	0.066	0.045	-0.067	0.041	0.005	0.327	-0.194	-0.151
WSe <sub>2</sub>	3.325	0.860	1.892	-0.152	-0.125	0.508	0.094	0.129	0.009	0.044
	-0.278	0.129	0.059	0.058	-0.090	0.039	0.001	0.392	-0.224	-0.165
MoTe <sub>2</sub>	3.357	0.574	1.410	-0.148	-0.173	0.333	0.203	0.186	0.127	0.007
	-0.280	-0.067	0.073	0.081	-0.054	0.008	0.037	0.145	-0.078	0.035
WTe <sub>2</sub>	3.560	0.675	1.489	-0.124	-0.159	0.362	0.196	0.101	0.044	-0.009
	-0.250	0.129	0.131	-0.007	-0.086	0.012	-0.020	0.361	-0.193	-0.129

Table B.2: Fitted parameters in three-band TNN TBM for both GGA and LDA cases for MX<sub>2</sub> [1].

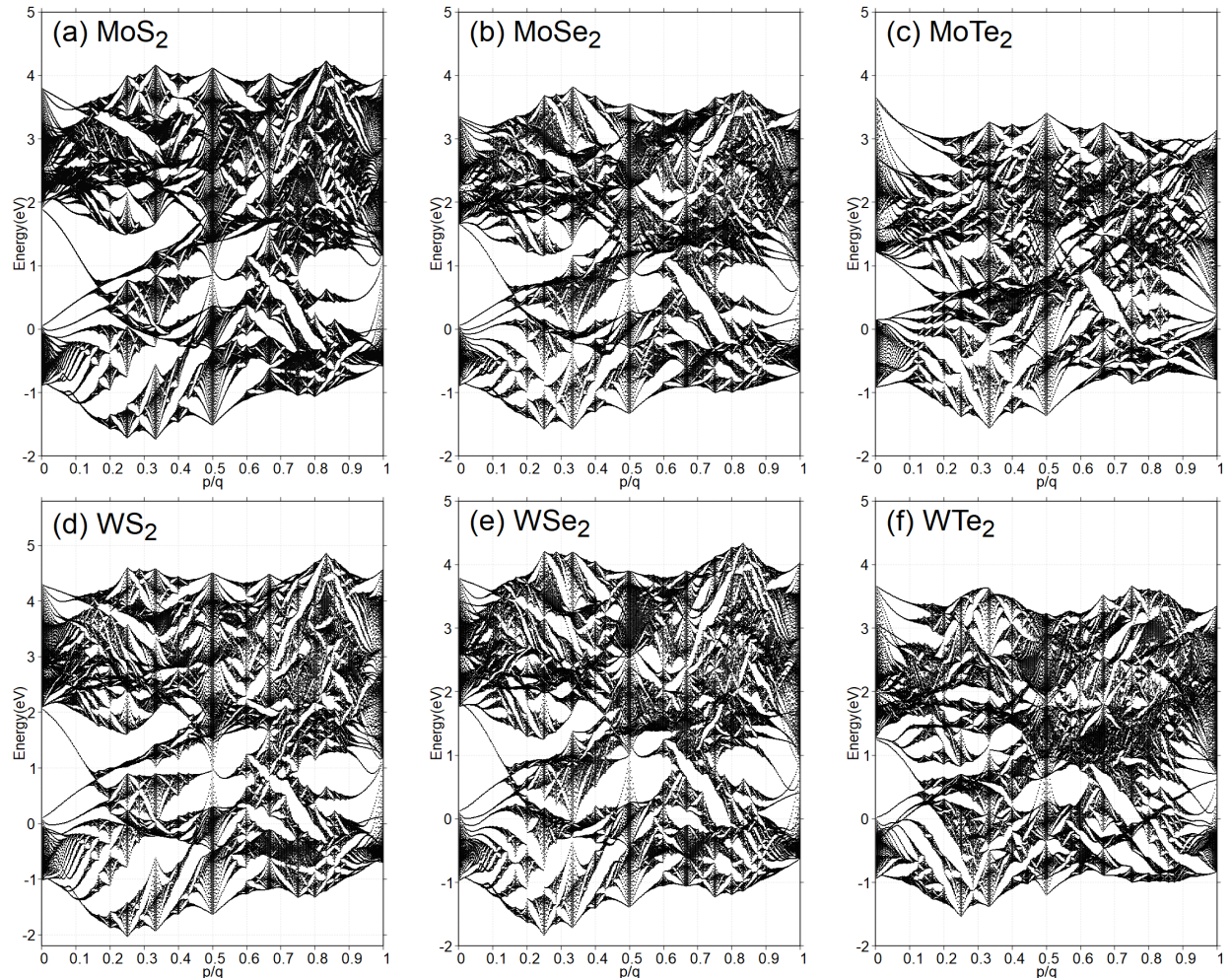


Figure B.2: The TNN Hofstadter's butterflies of  $\text{MX}_2$  monolayers using GGA parameters from Table B.2.

## APPENDIX C

### Details of the Peierls substitution

As we mentioned in Section 3.2, we work in the Landau gauge  $\mathbf{A} = (By, 0, 0)$ . The Peierls phase is given as  $\theta_{i,i'} = \int_i^{i'} \mathbf{A} \cdot d\mathbf{r}$ . By making an parametrization, for instance

$$\begin{cases} x = x_m + (x_{m'} - x_m)\tau, \\ y = y_n + (y_{n'} - y_n)\tau, \end{cases} \quad (\text{C.1})$$

where  $\tau \in [0, 1]$  and  $i = (m, n)$ , thanks to the Landau gauge, the path integral resembles to  $\int Bx dy$ , the phases can be written as

$$\begin{aligned} \theta_{i,i'} &= \frac{eB}{\hbar} \int_0^1 [x_m + (x_{m'} - x_m)\tau] (y_{n'} - y_n) d\tau \\ &= \frac{eB}{\hbar} \left( x_m + \frac{x_{m'} - x_m}{2} \right) (y_{n'} - y_n) \\ &= \frac{eB}{\hbar} \left( \frac{x_m + x_{m'}}{2} \right) (y_{n'} - y_n). \end{aligned} \quad (\text{C.2})$$

From this, the Peierls phase depends on absolute  $x$  coordinates but only relative to  $y$  coordinates.

## APPENDIX D

### Solving the Diophantine equation

We have defined the magnetic flux through a unit cell is  $\frac{\Phi}{\Phi_0} = \frac{p}{q}$ . Given  $p$  and  $q$  are mutually prime numbers, we set the pairs  $(\nu_r, s_r) = (m, n)$  as the solution of the Diophantine equation.

$$pm + qn = r. \quad (\text{D.1})$$

By using Euclidean algorithm, we can obtain  $(m, n)$ . For instance, taking the rational flux ratio is  $p/q = 4/13$ , thus the Chern number goes from  $-6$  to  $6$ , and the equation (D.1) becomes

$$r = 4m + 13n. \quad (\text{D.2})$$

In the meantime, the gap index  $n$  now varies from  $-q$  to  $q$  due to the butterfly's symmetry. Each value of  $r$ , going from  $0$  to  $q - 1$  only have one couple of valid  $(m, n)$ . The values of  $r$  are depicted in Table D.1

$r$	0	1	2	3	4	5	6	7	8	9	10	11	12
$m$	0	-3	-6	4	1	-2	-5	5	2	-1	-4	-6	3
$n$	0	1	2	-1	0	1	2	-1	0	1	2	-1	0

Table D.1: Allowed values of  $r$ .

## REFERENCES

- [1] Gui-Bin Liu, Wen-Yu Shan, Yugui Yao, Wang Yao, and Di Xiao. Three-band tight-binding model for monolayers of group-vib transition metal dichalcogenides. *Phys. Rev. B*, 88:085433, Aug 2013.
- [2] Yen-Hung Ho, Yi-Hua Wang, and Hong-Yi Chen. Magnetoelectronic and optical properties of a mos 2 monolayer. *Physical Review B*, 89(15):155316, 2014.
- [3] Yen-Hung Ho, Wu-Pei Su, and Ming-Fa Lin. Hofstadter spectra for d-orbital electrons: a case study on mos 2. *Rsc Advances*, 5(27):20858–20864, 2015.
- [4] K. v. Klitzing, G. Dorda, and M. Pepper. New method for high-accuracy determination of the fine-structure constant based on quantized hall resistance. *Phys. Rev. Lett.*, 45:494–497, Aug 1980.
- [5] Di Xiao, Ming-Che Chang, and Qian Niu. Berry phase effects on electronic properties. *Reviews of modern physics*, 82(3):1959–2007, 2010.
- [6] Li F Mattheiss. Band structures of transition-metal-dichalcogenide layer compounds. *Physical Review B*, 8(8):3719, 1973.
- [7] Rudolph Peierls. Zur theorie des diamagnetismus von leitungselektronen. *Zeitschrift für Physik*, 80(11):763–791, 1933.
- [8] Fırat Yalçın. Tight binding investigation of graphene nanostructures under magnetic field. Master’s thesis, Middle East Technical University, 2019.
- [9] Douglas R. Hofstadter. Energy levels and wave functions of bloch electrons in rational and irrational magnetic fields. *Phys. Rev. B*, 14:2239–2249, Sep 1976.
- [10] Juan Li, Yi-Fei Wang, and Chang-De Gong. Tight-binding electrons on triangular and kagomé lattices under staggered modulatedmagnetic fields: quantum hall effects and hofstadter butterflies. *Journal of Physics: Condensed Matter*, 23(15):156002, 2011.
- [11] Yakir Aharonov and David Bohm. Significance of electromagnetic potentials in the quantum theory. *Physical review*, 115(3):485–497, 1959.

- [12] R Rammal. Landau level spectrum of bloch electrons in a honeycomb lattice. *Journal de Physique*, 46(8):1345–1354, 1985.
- [13] D. Shoenberg. *Magnetic Oscillations in Metals*. Cambridge Monographs on Physics. Cambridge University Press, 1984.
- [14] J. Singleton. *Band Theory and Electronic Properties of Solids*. Oxford Master Series in Condensed Matter Physics. OUP Oxford, 2001.
- [15] S. Blundell. *Magnetism in Condensed Matter*. Oxford Master Series in Condensed Matter Physics 4. OUP Oxford, 2001.
- [16] C. Kittel. *Quantum Theory of Solids*. Wiley, 1987.
- [17] Mahito Kohmoto. Zero modes and the quantized hall conductance of the two-dimensional lattice in a magnetic field. *Physical Review B*, 39(16):11943, 1989.
- [18] Yasuhiro Hatsugai and Mahito Kohmoto. Energy spectrum and the quantum hall effect on the square lattice with next-nearest-neighbor hopping. *Physical review B*, 42(13):8282, 1990.
- [19] Mahito Kohmoto. Topological invariant and the quantization of the hall conductance. *Annals of Physics*, 160(2):343–354, 1985.
- [20] D. J. Thouless, M. Kohmoto, M. P. Nightingale, and M. den Nijs. Quantized hall conductance in a two-dimensional periodic potential. *Phys. Rev. Lett.*, 49:405–408, Aug 1982.
- [21] P Streda. Theory of quantised hall conductivity in two dimensions. *Journal of Physics C: Solid State Physics*, 15(22):L717, 1982.
- [22] Francesco Di Colandrea, Alessio d’Errico, Maria Maffei, Hannah M Price, Maciej Lewenstein, Lorenzo Marrucci, Filippo Cardano, Alexandre Dauphin, and Pietro Massignan. Linking topological features of the hofstadter model to optical diffraction figures. *New Journal of Physics*, 24(1):013028, 2022.
- [23] Itzhack Dana, Yosi Avron, and J Zak. Quantised hall conductance in a perfect crystal. *Journal of Physics C: Solid State Physics*, 18(22):L679, 1985.
- [24] Joseph E Avron, Daniel Osadchy, and Ruedi Seiler. A topological look at the quantum hall effect. *Physics today*, 56(8):38–42, 2003.